LAWRENCE
LIVERMORE
NATIONAL
LABORATORY

LLNL-JRNL-404606

The Blast-Wave-Driven Instability as a Vehicle for Understanding Supernova Explosion Structure

A. R. Miles

June 11, 2008

Astrophysical Journal

Disclaimer

THE BLAST-WAVE-DRIVEN INSTABILITY AS A VEHICLE FOR UNDERSTANDING SUPERNOVA EXPLOSION STRUCTURE

AARON R. MILES

Lawrence Livermore National Laboratory, Livermore, CA 94550;

miles15@llnl.gov

ABSTRACT

Blast-wave-driven instabilities play a rich and varied role throughout the evolution of supernovae from explosion to remnant, but interpreting their role is difficult due to the enormous complexity of the stellar systems. We consider the simpler and fundamental hydrodynamic instability problem of a material interface between two constant-density fluids perturbed from spherical and driven by a divergent central Taylor-Sedov blast wave. The existence of unified solutions at high Mach number and small density ratio suggests that general conclusions can be drawn about the likely asymptotic structure of the mixing zone. To this end we apply buoyancy-drag and bubble merger models modified to include the effects of divergence and radial velocity gradients. In general, these effects preclude the true self-similar evolution of classical Raleigh-Taylor, but can be incorporated into a quasi-self-similar growth picture. Loss of memory of initial conditions can occur

in the quasi-self-similar model, but requires initial mode numbers higher than those predicted for pre-explosion interfaces in Type II SNe, suggesting that their late-time structure is likely strongly influenced by details of the initial perturbations. Where low-modes are dominant, as in the Type Ia Tycho remnant, they result from initial perturbations rather than generation from smaller scales. Therefore, structure observed now contains direct information about the explosion process. When large-amplitude modes are present in the initial conditions, the contribution to the perturbation growth from the Richtmyer-Meshkov instability is significant or dominant compared to Rayleigh-Taylor. Such Richtmyer-Meshkov growth can yield proximity of the forward shock to the growing spikes and structure that strongly resembles that observed in the Tycho. Laser-driven high-energy-density laboratory experiments offer a promising avenue for testing model and simulation descriptions of blast-wave-driven instabilities and making connections to their astrophysical counterparts.

Subject headings: hydrodynamics – instabilities – supernovae: general – supernovae: individual (Tycho) – supernova remnants

1. INTRODUCTION

Supernovae are among the most dramatic explosions in the universe. Type II supernovae follow the core collapse of a massive star (Wheeler 1996), while Type Ia supernovae are typically believed to be thermonuclear explosions of carbon-oxygen white dwarfs that have accreted enough material to initiate carbon burning (Hoyle and Fowler 1960; Nugent *et al.* 1997; Hillebrandt and Niemeyer 2000). In both cases, the explosion dynamics are complicated by hydrodynamic instabilities that make spherical symmetry impossible. In core collapse supernovae, instabilities driven by the supernova blast wave can mix heavy core elements into the outer layers, making them observable much earlier than would be predicted by one-dimensional models (Falk and Arnett 1973; Chevalier 1976; Fryxell *et al.* 1991). This mechanism has been invoked to help explain observations of SN1987A, in which heavy core elements (in particular ^{56}Ni produced in Si burning) were observed at the photosphere within five days after core collapse rather than after six months as predicted by 1D models (Blinnikov *et al.* 2000; Mitchell *et al.* 2001; Muller *et al.* 1991; Tueller *et al*., 1990). To date, 2D SN simulations have reduced the predicted ^{56}Ni observation time from months down to days, but most produce heavy metal velocities that are still low by about a factor of two (Kifonidis *et al.* 2003; Muller *et al.* 1991). In the calculations by Kifonidis *et al.*, neutrino-driven convection perturbs the inner Si/O interface, and these perturbations are driven unstable with the passage of the outgoing blast wave. The instabilities produce long spikes of heavy core material with velocities

that are initially high enough, but these fast spikes are decelerated when they collide with the dense He layer that has formed after shock transmission through the He/H interface. They dissipate energy in shocks and are decelerated down to about half the observed velocities. The He/H layer, though unstable, was not perturbed in this calculation, leaving open the possibility that its instability might lead to breakup of the shell and allow fast inner spikes to escape undecelerated. Another important question is whether differences in 3D vs 2D spike velocities are important, or differences between the growth of turbulent mixing zones and 2D laminar simulations. Finally, can special choices of the initial perturbation spectrum allow inner material to escape before the formation of the He shell? Indeed, more recent calculations by Kifonidis *et al.* (2006) do yield metal velocities that are high enough due to the early presence of kinked shocks and resultant shock-driven Richtmyer-Meshkov (RM) instabilities (Meshkov 1969; Richtmyer 1960). The RM instability is the growth of perturbations on a material interface due to vorticity deposited by a transmitted shock. While the RM instability is typically considered for planar shocks transmitted through perturbed interfaces, it is important to note that growth depends on obliqueness of the shock relative to the interface, whether the initial perturbation is on the interface or the shock front.

In thermonuclear supernovae, many details of the combustion process remain unanswered, and a number of different models have been considered.

These include detonation (Arnett 1969), deflagration (Ivanova *et al.* 1974; Nomoto *et al.* 1976), and delayed detonation (Khokhlov 1991). Delayed detonation models involve a transition from an initial deflagration phase to a detonation phase that is initiated in an ad hoc fashion or via a posited physical mechanism, as in the pulsating delayed detonation (PDD) (Ivanova *et al.* 1974; Khokhlov 1991), pulsating reverse detonation (PRD) (Bravo and Garcia-Senz 2006), and gravitationally confined detonation (GCD) (Plewa *et al.* 2004) models. In any model where deflagration is important, the evolution of Rayleigh-Taylor (RT) (Rayleigh 1899; Taylor 1950) unstable flames influences the rate of combustion and the final composition of the remnant (see, for example, Khokhlov 1995 and references therein).

For any type of supernova, the expanding ejecta are eventually decelerated by the circumstellar medium, driving additional Rayleigh-Taylor growth (Gull 1973). The 400-year-old Tycho supernova remnant, believed to be the result of a Type Ia explosion, provides a dramatic example of this process. In x-ray images taken by the *Chandra* observatory, instability-driven spikes of heavy material are clearly visible and have grown out to the forward shock, which is also highly perturbed (Warren *et al.* 2005). These images raise a number of questions, particularly because current multidimensional remnant simulations predict that the shock would have pulled away from the developing RT spikes before the present time (Dwarkadas 2000; Wang and Chevalier 2001). Some have suggested that this

discrepancy could be resolved by large-scale density inhomogeneities in the circumstellar medium (Jun *et al.* 1996) or high-density-contrast clumps in the ejecta (Wang *et al.* 2001). Others point to evidence of cosmic ray acceleration behind the forward shock as a means of effectively increasing the compressibility of the material between the shock and interface and thereby reducing their separation (Decourchelle *et al.* 2000; Blondin and Ellison 2001).

A general question for all of these shock-driven RT-unstable divergent systems is what determines the late-time asymptotic structure of the mixing region? How does this structure depend on the driving accelerations, the radial density profile, and the initial perturbations that seed the instability growth?

The apparent relevance of shock and blast-wave-driven hydrodynamic instabilities to supernova dynamics has led to interactions between the astrophysics, compressible turbulent mixing, high-energy-density (HED) physics, and inertial confinement fusion (ICF) communities. In particular, laboratory HED and ICF systems routinely confront researchers with material interfaces driven unstable by interactions with shock and blast waves. Reflecting the background of these communities, much of the work that is done on hydrodynamic mixing in SNe draws, on the one hand, on the fundamental instability problems of classical RT and steady-shock RM, and, on the other hand, on complex, often multiphysics computational and experimental systems. These include numerical simulations of supernovae and laser-driven laboratory experiments that invoke Euler scaling to

make connections to their much larger astrophysical counterparts (Ryutov *et al.* 1999; Remington *et al*. 2006 and references therein).

In this paper, we consider what additional insight is to be gained from considering what is really a third fundamental instability problem that is more relevant than either RT or RM in isolation and somewhat less complex than the full system. Namely, we consider an idealized blast-wave-driven problem in which a localized source drives a spherical Taylor-Sedov blast wave that in turn drives a perturbed interface between heavier and lighter gamma-law fluids. Within this context, we use numerical simulations and simplified analytic models to consider the effect of the initial perturbation spectrum in determining the late-time asymptotic state of the mixing zone and the proximity of the forward shock to the developing instability. We consider possible implications for both core collapse and thermonuclear supernovae. Finally, we discuss how laser-driven laboratory experiments might be used to help resolve some as yet unanswered questions in supernova explosion hydrodynamics.

2. IDEALIZED BLAST-WAVE-DRIVEN INSTABILITY (BWI)

In the spherical idealized blast-wave-driven instability (BWI) problem (see Fig. 1), a perturbed interface separates a ball of denser fluid with initial

radius r_0 and density ρ_1 from a lower-density ambient medium with density ρ_2. The central portion of the dense fluid (out to piston radius r_p) is initialized with a high overpressure P and corresponding high temperature T and energy E. At time zero, this piston region begins to expand and drive a shock into the surrounding high-density fluid. If the mass outside the piston is large compared to the mass of the piston region (or $r_p << r_0$), then the outgoing shock develops into a spherical Taylor-Sedov blast wave (Taylor 1950; Sedov 1946a; 1946b) before reaching the perturbed interface. In that case, the unperturbed problem is characterized by four dimensional parameters: the radius r_0, the density or mass of the ball, the density of surrounding fluid, and the drive overpressure (or energy or temperature). We define the density ratio $\eta \equiv \rho_2/\rho_1$, which we typically take to be not only less than one but much less than one. The problem specification is completed by giving the interface perturbation and the adiabatic indices of the two fluids, γ_1 and γ_2.

The dynamics of the blast-wave-driven interface are illustrated in Fig. 2 with a radius vs. time (r-t) diagram from a one-dimensional simulation performed with the hydrodynamics code CALE (Barton 1985). In this case, we pick an overpressure of 10^9 and an interface position that is 10 times greater than the piston radius. At the time it reaches the interface, the driving blast wave has a Mach number of 1800. The logarithm of the density is shown in grayscale, making visible the space-time trajectories of interfaces and waves. The outermost discontinuity is the blast wave shock propagating through the lighter material, and

the white line denotes the interface between the two fluids. The interface is shock accelerated and, because of the large density difference, is largely unaffected by the ambient fluid very early on. The interface then begins an RT-unstable deceleration due to the presence of the low-density ambient fluid, and a reverse shock is formed in the heavy fluid. Once the expanding interface has swept up a mass of low-density material that approaches the mass of high-density fluid, the reverse shock begins to propagate back toward the center, where it bounces and comes back again as a reflected shock. At a radius of about 1.5 times this equal mass point, the interface expansion is halted (or nearly halted), and it in many cases begins to fall back until it is reshocked by the reflected reverse shock. At late times, the main shock and the interface both expand with Taylor-Sedov blast wave scaling.

In the SNR literature, the early constant-velocity phase is called the ejecta-dominated (ED) phase while the extended late-time period is called the Taylor-Sedov (TS) phase (or Sedov-Taylor) (Chevalier 1977). The two are separated by a more complicated intermediate phase that we will refer to as "the intermediate phase" or "fast growth phase". The interface is unstable during the limited fast-growth phase and the more extended Taylor-Sedov or slow-growth phase. As is apparent from Fig. 2, the equal-mass radius is the governing length scale in the blast-wave-driven interface problem.

The development of the instability is illustrated in Fig. 3, which includes log density images from a 2D RAPTOR simulation at several points in its evolution, each of which is labeled with its dimensionless time $\tau \equiv t/t_m$ (t_m is the equal mass time defined below) and interface radius $\xi \equiv r_i/r_m$. RAPTOR is an Eulerian Adaptive Mesh Refinement code that uses a second-order accurate (in space and time) Godunov method to numerically solve the Euler equations (Howell and Greenough 2003). In this simulation, $\eta = 0.01$ and the interface is seeded with a narrow Gaussian perturbation spectrum centered at mode 160 with width 20. The characteristic mode 160 is initially marginally linear with $kh_0 = 1/3$. The incident blast wave crosses the interface at $\tau \approx 0.2$ between Figs. 3a and 3b, initiating the short-lived ED phase. The perturbations grow during the intermediate phase into outward "falling" spikes of material 1 and inward "rising" bubbles of material 2 as the interface approaches the equal-mass radius and begins to decelerate dramatically. The reverse shock forms and begins to propagate back towards the center in Fig. 3c when the interface has expanded to about the equal-mass radius, where it converges in Fig. 3d. In Fig. 3e, the reflected reverse shock returns to the developing mixing zone, which is reshocked in Fig. 3f. This second shock exits the mixing zone in Fig. 3g on its way to overtake the main shock, having set a very complicated initial condition for the ensuing TS phase. At this point, considering the differences observed in 3D vs 2D simulations of blast-wave-driven interfaces, we can't really believe this 2D calculation's prediction of

the internal structure of the mix region, and only suggest that there might not be anything left for the instability to act on during the TS phase.

3. SELF-SIMILAR AND UNIFIED SOLUTIONS

During the ED and TS phases, the unperturbed blast-wave-driven interface problem is characterized by only two dimensional parameters for small η and while the Mach number of the shock is high. In the ED phase, the ambient fluid density ρ_2 drops out and the initial interface motion is determined by the pressure incident upon it rather than the full drive pressure, so we are left with ρ_1 and $P_0 \sim E/r_0^3$. In the TS phase, the initial radius is small compared to the instantaneous interface and shock radii, and the mass of swept-up low-density fluid is much larger than the mass of high-density fluid, leaving only the drive pressure and the ambient fluid density. With only two dimensional parameters, the Euler equations admit a self-similar solution in which all the fluid fields depend on a single variable that is a combination of the two dimensional parameters and the space and time coordinates (Sedov 1959).

If there are three independent dimensional parameters instead of two, the result is what Truelove and McKee (1999) have referred to as a "unified solution". When written in dimensionless form using the correct spatial and

temporal scaling, a unified solution is still independent of the characteristic dimensional parameters (Sedov 1992). That is, radial profiles evolve in dimensionless time and space, but profiles from two systems with different values of the three dimensional parameters differ only by a scale factor when viewed at the same dimensionless time. The classic example is the evolution of the Taylor-Sedov blast wave to the point that the ambient pressure is no longer negligible (the so-called point explosion with counter pressure), and so enters as the third dimensional parameter in addition to the energy and ambient density (Sedov 1959; 1992).

Like the very closely related nonradiative SNR problem (McKee and Truelove 1995; Truelove and McKee 1999), the blast-wave-driven interface problem qualifies for a unified solution, from the ED stage through the intermediate phase and into the TS phase, if the density difference is very large, or equivalently, if r_0 is very small compared to the equal mass radius. The three remaining dimensional parameters are the heavy-fluid densities or mass, the drive pressure or energy, and the initial interface radius. The unified nature of the blast-wave-driven interface can be illustrated in a number of different ways. In Fig. 4, we show r-t diagrams from 1D CALE simulations of a spherical blast-wave-driven interface with four different values of the density ratio η ranging from unity (equal densities) to 0.001. In each plot, the radial and time dimensions are scaled by the equal-mass radius and time:

$$r_m \equiv \eta^{-1/3}(1+\eta)^{1/3} r_0 \tag{1a}$$

$$t_m \equiv \sqrt{\frac{r_m^5 \rho_2}{E}} = \eta^{-1/3}(1+\eta)^{5/6}\sqrt{\frac{r_0^5 \rho_1}{E}} = \eta^{-5/6}(1+\eta)^{5/6}\sqrt{\frac{r_0^5 \rho_2}{E}} \tag{1b}$$

Up to an order-unity constant factor, the equal-mass time is that at which the TS blast wave would reach the equal-mass radius if propagating through just the ambient material. To lowest order in the density ratio, these agree with the characteristic radius and time reported by Truelove and McKee (1999) for the nonradiative remnant. Because of the unified nature of the problem, the scaled r-t plots in Fig. 4 look the same at low η. Of course as the density ratio approaches one, the scaled solution must transform into the Taylor-Sedov blast wave and, over some region, the unified solution is not valid.

If we move from 1D to 2 and 3D, we might expect that the existence of a dimensionless unified solution implies dimensionless instability growth as long as the initial perturbations are scaled with r_0, as claimed by Chevalier *et al.* (1992) and Truelove & McKee (1999). Drive-energy independence is illustrated in Fig. 5, where we show log density plots from two RAPTOR simulations that are identical except that the drive energy differs by a factor of 100. The systems are shown at the same scaled time and, although the physical time differs by a factor of 10, the developing instability looks qualitatively the same in the two systems. Before discussing dependence of the scaled instability growth on the density ratio, we first turn to analytic modeling of the nonlinear phase of instability evolution.

4. BUOYANCY-DRAG MODEL FOR THE BLAST-WAVE-DRIVEN INTERFACE

Blast-wave-driven systems differ from classical RT in three important aspects: the RM component, compressibility, and the time dependence of the driving acceleration. The most important compressibility effect is the growth of perturbations due to material decompression in the rarefaction behind the shock front. We can incorporate this perturbation stretching into the simplest of models by starting with a buoyancy-drag (BD) model, which gives the acceleration of nonlinear bubbles or spikes due to a buoyancy term and a drag term (Davies and Taylor 1950; Hanson *et al.* 1990; Dimonte and Schneider 1996; Oron *et al.* 2001), and adding on a third term to account for the decompression (Miles 2004). The equation for bubbles is

$$\frac{d}{dt}\frac{dh(t)}{dt} = \tilde{A}(t)g(t) - \frac{\tilde{C}}{\lambda}u_{inst}(t)^2 + \frac{d}{dt}\omega(t)h(t). \qquad (2)$$

In equation (1), $\tilde{A}$ is the post-shock modified Atwood number $\tilde{A} \equiv A\left(1+\eta^*\right)/\left(C_a+\eta^*\right)$ where the post-shock Atwood number is given by $A = \left(1-\eta^*\right)/\left(1+\eta^*\right)$, $\tilde{C}$ is the modified drag coefficient $\tilde{C} \equiv C/\left(C_a+\eta^*\right)$, the drag coefficient is approximately given by $C = 2\pi\{3,1.22\}_{2D,3D}$ (Davies and Taylor

1950; Layzer 1955), the added mass coefficient $C_a = \{2,1\}_{2D,3D}$, $g(t)$ is the interface acceleration, $u_{inst}(t)$ is the bubble or spike speed relative to the background fluid, and $\lambda(t)$ is the perturbation wavelength, in which the time-dependence accounts for transverse stretching due to divergence. Here and throughout, we use asterisks to denote post-shock densities and density ratios. The equation for spikes is obtained from equation (2) simply by replacing η^* with $1/\eta^*$. In the third term,

$$\omega(t) \equiv \left[\frac{\partial u(r,t)}{\partial r}\right]_{r=r_i(t)} \tag{3}$$

is the velocity gradient evaluated at the instantaneous interface position. In a previous publication, we constructed such a model under certain limiting assumptions, most notably by focusing on the case where $u = (\beta/\gamma)\cdot r/t$, which applies during the TS phase (Miles 2004). The u_{inst} term recognizes the fact that the bubble or spike velocity in the rest frame of the unperturbed interface consists of two parts,

$$\frac{dh}{dt} = u_{inst}(t) + \omega(t)h(t) \tag{4}$$

where u_{inst} is the instability velocity due to RT and RM, and the second term is a background (de)compression contribution. When equation (4) is inserted into equation (2), the compression terms cancel and we are left with a standard buoyancy-drag equation:

$$\frac{du_{inst}}{dt} = \tilde{A}g(t) - \frac{\tilde{C}}{\lambda}u_{inst}(t)^2 \qquad (5)$$

for the evolution of the instability velocity. Equation (5) can thus be solved first for $u_{inst}(t)$, and the solution inserted into equation (4), which can then be integrated to find the total perturbation growth:

$$H(t) = h^* + \int_{t_0}^{t} dt e^{-\int_{t_0}^{t'} \omega(t'')dt''} u_{inst}(t'), \qquad (6)$$

where h^* is the post-shock initial amplitude and we have defined the modified amplitude function

$$H(t) \equiv h(t)Exp\left[-\int_{t_0}^{t} \omega(t')dt'\right]. \qquad (7)$$

In some cases, a simplified analytic form of $u_{inst}(t)$ is justified. Two which are routinely used in application of BD models are that of impulsive acceleration (Shvarts *et al.*1995; Alon *et al.* 1994, Oron *et al* 2001) and terminal-velocity RT (Davies and Taylor 1950; Oron *et al* 2001). In the impulsive-acceleration case, corresponding to nonlinear RM, $g(t) = u_0\delta(t - t_0)$ and the drag term provides deceleration according to

$$u_{inst}(t) = \frac{u_0}{1 + \frac{\tilde{C}}{\lambda(t)}u_0(t - t_0)} = \frac{u_0}{1 + \tilde{C}m_0\frac{u_0(t - t_0)}{2\pi r_i(t)}}. \qquad (8)$$

Within the simplest impulsive model of Richtmyer (1960), or as modified by Meyer and Blewett (1972) for the heavy-to-light case, $u_0 = k_0 a_0 A u_{i0}$ where

$k_0 = m_0 / r_0$ is the initial wavenumber, $a_0 \equiv \left(h_0 + h^*\right)/2$, and h_0 is the initial pre-shock amplitude.

In the terminal velocity RT model, commonly applied to nonlinear RT bubbles, buoyancy and drag balance one another to give

$$u_{inst}(t) = \sqrt{\frac{2A}{(1 \pm A)C}\lambda(t)g(t)} = \sqrt{\frac{2A}{(1 \pm A)C}\lambda_0 \frac{r(t)g(t)}{r_0}}, \tag{9}$$

where the plus and minus signs are for bubbles and spikes, respectively.

Finally, since spikes at high Atwood number might grow significantly before approaching terminal velocity, a free-fall model wherein drag is neglected might be useful:

$$u_{inst}(t) = Au_{i0}\left[k_0 a_0 + \frac{1+\eta^*}{C_a + \eta^*}\left(1 - \frac{u_i(t)}{u_{i0}}\right)\right]. \tag{10}$$

Unlike the previous two simplified models, the free-fall model includes contributions from both RT and RM, the latter through an initial post-shock growth velocity. The terminal velocity BD model cannot include an RM contribution because by assumption the growth velocity at any time is proportional to the square root of the instantaneous acceleration.

Inserting the terminal-velocity RT instability velocity into equation (6), we find

$$H(t) = h^* + \sqrt{\frac{\lambda_0 r_0}{C}} f_{BD}(t) \tag{11a}$$

$$\frac{h(t)}{r_i(t)} = \left(\frac{h^*}{r_0} + \sqrt{\frac{\lambda_0}{C r_0}} f_{BD}(t) \right) \frac{1}{q(t)}, \tag{11b}$$

where we have defined the BD growth and stretch functions:

$$f_{BD}(t) \equiv \int dt' e^{-\int \omega dt} \sqrt{A(t') r(t') g(t')} / r_0 \tag{12}$$

$$q(t) \equiv e^{-\int \omega dt} \frac{r_i(t)}{r_0}. \tag{13}$$

Significantly, where the unified solution to the 1D problem is valid, strict unified instability growth requires that both f_{BD} and q are unified, while approximately unified growth of short wavelength modes requires only that the ratio f_{BD}/q is unified. In fact, since the growth and stretch functions contain quantities that are not normalized to the equal-mass radius and time, we should not expect them to be unified. In Fig. 6, we plot the scaled evolution of several relevant functions at a wide range of density ratios and two different piston radii. The idea is to see which are unified, at least up to small differences in the post-shock Atwood number. Figure 6a shows that the exponential decompression function appearing in both equations (12) and (13) is not unified. Instead, it is proportional to r_m/r_0 (Fig. 6b). Based on the structure of the growth and stretch functions, this implies that f_{BD} and q are not unified, but the product of either one and $(r_0/r_m)^2$ is (see Fig. 6c-6e). Therefore, the ratio f_{BD}/q is unified as well (Fig. 6f).

Consequently, nonlinear single-mode RT bubble growth in the BWI as predicted by the BD model is not strictly unified, but is approximately unified for short-wavelength modes scaled with r_0. In addition to small differences in the post-shock Atwood number that come with different pre-shock density ratios, this conclusion also neglects the effect of the density ratio on the factor by which perturbation amplitudes are compressed by the shock as it is transmitted through the interface. This does not introduce an additional limitation on when unified single-mode perturbation growth may arise, however, since we already require that the initial amplitude term in equation (11) be comparatively small. Nevertheless, we always include the η-dependent shock-compression factor in actual implementation of the buoyancy-drag model.

5. BUBBLE-MERGER MODEL

Because larger bubbles rise faster than smaller bubbles and a larger bubble rising above its smaller neighbors is free to expand laterally, nonlinear RT is characterized by an inverse cascade to larger and larger structures (Sharp 1984; Glimm and Li 1988). In the case of constant acceleration, this results in an ever-increasing instability growth rate.

Bubble merger models represent this inverse cascade as the merger of one generation of bubbles (of some size) into a succeeding generation of larger bubbles (Sharp 1984; Glimm and Li 1988). This can in principle result in self-similar instability growth that is independent of the initial perturbation spectrum – in which case we say that memory of the initial conditions has been lost (Youngs 1984). The higher the driving acceleration, the shorter the merger time at the i^{th} generation, which is defined as the time at which the i^{th} merger is complete minus the time at which it begins. Even in classical RT (incompressible, constant acceleration), the merger time grows larger with each successive generation as the bubble diameter λ_i increases [$\tau_i = t_{i+1} - t_i \sim \sqrt{\lambda_i g}$ (Sharp 1984; Glimm and Li 1988; Alon *et al.* 1994)]. In a blast-wave-driven system, the driving acceleration decays away in time, and so the time to generate each successive generation of larger bubbles grows much, much faster than in classical RT (Miles 2004).

In classical multimode RT, self-similarity reduces to $h(t) \propto \lambda(t) \propto gt^2$ and is attained after many generations of bubble merger (Sharp 1984). Instead of defining a merger law and evolving the model, we can get the same result by starting with a similarity ansatz and using it to replace $\lambda(t)$ in the terminal velocity model (Shvarts *et al.*1995; Alon *et al.* 1994). Guided by the structure of the BWI BD equation and our previous work, we assume a quasi-self-similarity (QSS) ansatz

$$\lambda(t) = \sigma h(t) e^{-\int \omega dt} \frac{r(t)}{r_0} = \sigma h(t) q(t). \qquad (14)$$

Self-similarity can then be modified through the exponential factor, which describes decompression, and $r(t)/r_0$, which accounts for divergence. The stretch function $q(t)$ defined in equation (13) in the context of single-mode growth now appears as a quasi-self-similarity function that describes deviations from classical self-similarity. In a system with divergence but no stretching, the ratio of wavelength to amplitude grows in proportion to the interface expansion factor. With stretching but no divergence, as with planar blast waves, the ratio decays in time. If $u = (\beta/\gamma) \cdot r/t$, as is approximately true in the TS phase with $\beta = 2/5$, then $r(t)/r_0 = e^{\int \omega dt}$ and true self-similar growth is possible.

When equation (14) is inserted into equation (4), which can then be rewritten

$$\frac{d\sqrt{H(t)}}{dt} = \frac{1}{2} Exp\left[-\int \omega dt\right] \sqrt{\frac{A\sigma}{C} \frac{r(t)}{r_0} g(t)}, \qquad (15)$$

the latter is integrated to give the quasi-self-similar growth solution

$$H(t) = \left[\sqrt{h^*} + \tfrac{1}{2\sqrt{C}} \int dt' e^{-\int \omega dt} \sqrt{\frac{r(t')}{r_0} A(t') g(t')}\right]^2. \qquad (16)$$

This same result can be obtained directly from a bubble-merger model without first assuming quasi-self-similarity when $u(r,t) \propto r/t$ (Miles 2004). Using the BD growth function equation (12), we find:

$$H(t) = \left[\sqrt{h^*} + \sqrt{\alpha r_0} f_{BD}(t)\right]^2 \tag{17}$$

$$m(t) = \left[\frac{1}{\sqrt{m_0}} + \sqrt{\alpha\sigma/2\pi} f_{BD}(t)\right]^{-2}, \tag{18}$$

where $\alpha \equiv \frac{\sigma}{4C}$ is the same self-similarity α of classical RT turbulent growth. In equation (18), *m(t)* is the perturbation mode number $2\pi r(t)/\lambda(t)$.

If the system succeeds in reaching an asymptotic state where the second term dominates, then memory of the initial conditions is lost:

$$H(t) \to \alpha\left[\int dt' e^{-\int \omega dt''} \sqrt{A(t')g(t')r(t')/r_0}\right]^2 \tag{19}$$

$$m(t) \to \frac{2\pi}{\alpha\sigma}\left[\int dt' e^{-\int \omega dt''} \sqrt{A(t')g(t')r(t')}/r_0\right]^{-2} \tag{20}$$

If we neglect divergence and stretching and assume constant acceleration, we recover the classical results $h(t) \to \alpha A g t^2$, $\lambda(t) = \sigma h(t)$.

6. MODEL LIMITATIONS AND IMPLEMENTATION

In applying the buoyancy-drag and QSS growth models developed above to the BWI, we are hindered by two significant model limitations. First of all, we have not accounted for the time- and space-dependent radial density gradient. Since the density gradient away from the interface is typically positive, spikes and

bubbles tend to see an Atwood number that is decreasing as the perturbation grows. The blast-wave-driven flow leads to the formation of high-density shells immediately behind the interface and the forward shock, and there are regions of large density gradient associated with each shell. The density gradient does not seem to be very important on the bubble side of the interface, since thin-shell RT growth (Ott 1972; Hurricane 2005) can continue once the bubble amplitude is comparable to and greater than the unperturbed shell thickness. It can provide the ultimate limit to spike growth, however, since spikes might eventually encounter a shell of material with density greater than their own. This effectively sets a maximum scaled spike amplitude that is set by the invariant density profile of the unified solution where it is applicable. We could in principle account for the density gradient by making the Atwood number dependent on both time and the perturbation amplitude. Since this makes the model so much more cumbersome, we instead typically ignore the effect on the bubble-side and limit the spike growth to the time-dependent width of the low-density shell ahead of the interface.

The second limitation is that the buoyancy-drag model assumes that perturbations are nonlinear, and the potential problem arises due to the fact that the velocity gradient at the interface is actually negative early on in the blast-wave-driven interface problem (see Fig. 7a). The exponential term in equation (14) is then positive, and QSS function $q = \lambda/\sigma h$ grows due to radial compression

in addition to divergence. As long as this condition is satisfied, the perturbation actually becomes more linear in time even as its amplitude grows. The effect of this error is well illustrated by the simple test case of constant acceleration, no divergence, and constant velocity gradient $\omega \equiv \pm\omega_0$, where $\omega_0 > 0$ so that the plus and minus signs denote positive and negative velocity gradient, respectively. The growth function and nonlinear single-mode growth are then given by $f_{BD} = \mp\sqrt{Ag/r_0}\left(e^{\mp\omega_0 t} - 1\right)/\omega_0$ and $h_{nl}(t) - h_0 e^{\pm\omega_0 t} = \mp\sqrt{A\lambda_0 g/C}\left(1 - e^{\pm\omega_0 t}\right)/\omega_0$. At very early times (to first-order in time), the velocity gradient is small and the classical result $h_{nl}(t) - h_0 = \sqrt{A\lambda_0 g/C}\,t$ is recovered. For positive velocity gradient, the late-time growth is exponential in time due to decompression. When the velocity gradient is negative, RT growth is eventually exactly compensated by compression and the amplitude asymptotes to a constant $h_{nl}(t) = \sqrt{A\lambda_0 g/C}\,/\omega_0$. Without divergence, the single-mode perturbation that is initially nonlinear will remain nonlinear for all time. The same is not always true in the QSS model, where the ratio of wavelength to amplitude is proportional to the QSS function $q = e^{\mp\omega_0 t}$. For negative velocity gradients, the perturbation becomes more linear exponentially in time. In our constant-velocity-gradient test problem, the QSS model then gives

$$h_\alpha(t) - h_{nl}(\pm\omega_0, t) = \alpha A g e^{\omega_0 t}\left(1 - e^{-\omega_0 t}\right)^2/\omega_0^2, \tag{21}$$

where the IC-independent quasi-self-similar term on the RHS is independent of the sign of the velocity gradient. The reason for the unlikely prediction that multimode perturbations growing in a fluid undergoing compression should evolve as fast as if the background fluid were expanding can be understood by considering the predicted wavelength growth, given by

$$\lambda_\alpha(t) = \left[\sqrt{\lambda_0} \mp \sqrt{\sigma\alpha Ag}\left(e^{\mp\omega_0 t} - 1\right)/\omega_0\right]^2. \tag{22}$$

For positive velocity gradient, we find the constant asymptotic limit $\lambda_\alpha(t) \to \left[\sqrt{\lambda_0} + \sqrt{\sigma\alpha Ag}\,/\omega_0\right]^2$ as expansion-driven growth eventually dominates instability-driven growth, while the negative gradient case tends to the exponentially-growing limit $\lambda_\alpha(t) \to \left(\sigma\alpha Ag/\omega_0^2\right)e^{2\omega_0 t}$. This exponentially-growing bubble diameter gives an exponentially-growing terminal velocity, and arises because the bubble-merger time tends to a wavelength-independent constant instead of the classical-RT behavior of growing with each successive generation of bubble merger. The end result is that the exponentially-growing terminal velocity compensates for the growing compression velocity. This behavior depends on an exponentially-growing ratio of bubble diameter to bubble height, and this same condition of course means that application of the nonlinear growth model and the terminal velocity on which it is based is not valid.

Wherever compression and/or divergence can give $kh < 1$, the inapplicability of the nonlinear model could be accounted for by including in the

terminal velocity a factor $\min\{1,\sqrt{(1+A)\pi C}h(t)/\lambda(t)\}$, which would give the smaller of the terminal velocity and the linear growth velocity. In order to again keep the perturbation amplitude out of the growth velocity and limit the complexity of the model, we instead simply hold the QSS q-function at unity while the velocity gradient is negative and once bubble merger has been initiated (see Fig. 7b). We consider this physically well-motivated since q-values greater than unity would imply bubble merger of linear perturbations while values smaller than unity would allow bubble merger that in compression would quickly return $q(t)$ back to unity.

When the initial amplitude is smaller than λ/σ, as in Fig. 7 where the model is applied to a system with $kh_0 = 1/3$ ($P/P_0 = 10^9$, $r_0/r_p = 10$, and $\eta = 0.01$), we evolve the perturbation according to the single-mode model until this bubble-merger threshold is reached. This single-mode phase gives $q > 1$ for $\xi < 0.42$ in Fig. 7b while holding the mode number in Fig. 7c at its initial value of 160.

Finally, the effect of the reflected reverse shock on the bubble growth is approximated under the simple assumption that bubble motion is halted when reshock is initiated. This produces a kink in the scaled perturbation amplitude predicted by both the nonlinear single-mode and multimode QSS models (see Fig. 7c). During the remainder of the fast growth phase, while the reflected reverse shock traverses the bubble region, the scaled amplitudes predicted by the model

decrease since the unperturbed interface radius is falling back towards the origin during this time (recall the discussion of Fig. 2).

For the asymptotic fast-growth-phase bubble amplitude and mode number, blue triangles in Fig. 7 denote results obtained from a 2D RAPTOR simulation. As in the simulation shown in Fig. 3, the initial perturbation spectrum is a narrow Gaussian centered at mode 160 that has a width of 20 modes with peak mode $k_{160}h_0 = 1/3$. The model reproduces the asymptotic mode number $m_{\alpha f} = 16$ observed in the simulation and comes within 10% of the scaled bubble amplitude at reshock (within 20% at the end of the fast-growth phase).

7. DEPENDENCE ON INITIAL CONDITIONS

The single-mode fast-phase growth predicted by the model is plotted in Fig. 8a for various density ratios (dashed curves) as a function of the initial characteristic mode number m_0. In the multimode case, the model predicts the asymptotic perturbation amplitude and the characteristic mode number. These expressions are plotted with the solid curves – the amplitude in Fig. 8a and the mode number in Fig. 8b. The dependence of the asymptotic ratio of bubble wavelength to amplitude is shown in Fig. 8c. If the initial amplitude is small and the initial mode number is high enough, the f_{BD}^2 terms in equations (17) and (18)

dominate and the asymptotic interface structure is independent of the initial conditions. An implicit consequence of equations (17) and (18) is that though loss of memory of initial conditions is possible during the fast-growth phase, it requires a high initial mode number due to the finite duration and decay of the driving acceleration as well as the requirement that several generations of bubble merger are required. A similar analysis can be carried out for the Taylor-Sedov phase slow growth, where the growth is limited by the finite lifetime of the driving blast wave, but it is the intermediate phase growth that is relevant for the early observation of core materials in Type II SNe. For example, the presence of the outgoing reflected shock in the Kifonidis *et al.* (2003) simulation shows that this is the end of the fast growth phase. In either phase, the model predicts that unless the initial mode number is quite high, memory of the initial perturbation is retained in both the parallel and transverse scales.

In Fig. 8, loss of memory of initial conditions is reflected in the flat portion of the QSS model curves. With our value of $\sigma = 4$, chosen to give $\alpha = 0.053$, the requirement is $m_0 > 100$ at $\eta \leq 0.01$and $m_0 > 10^4$ for $\eta = 0.1$. However, the asymptotic mode number is sufficiently small at very small η that it shows only weak dependence on the initial conditions down to $m_0 \sim 40$. Indeed, for a wide range of density ratios and initial mode numbers ranging from about 40 to greater than 10^4, the asymptotic mode number is predicted to be in the limited range of about 14-32. Since many 2D simulations are seeded either intentionally

or numerically with initial modes of order 100, it is not surprising that several groups find asymptotic structure characterized by modes ~20-32 and weak dependence on the initial perturbations. Such "preferred modes" are reported by Fryxell *et al.* (1991), Dwarkadas (2000), and Wang *et al.* (2001).

The QSS model predicts variation in asymptotic fast-phase interface structure as the density ratio is varied from 0.01 to 0.001. This suggests that multimode instability growth in the BWI is not strictly unified even when the 1D explosion dynamics is. However, the predicted variation is small enough that unified instability growth as a working assumption does not seem unreasonable.

For arbitrarily small initial amplitude and high mode number at $A = 1$, the QSS model gives $h_{\alpha f}/r_f \sim 0.5$ and $m_{\alpha f} \sim 16$. Thus these are the maximum bubble amplitude and minimum mode number arising from small-scale initial conditions that we would expect to see at the end of the fast-growth phase.

Simulations of Type II SNe and their progenitors predict relatively low modes ($m_0 \sim$ 20-50) in the initial conditions. Kifonidis *et al.* (2003) show $m_0 \sim 24$ due to neutrino-driven convection in the core, or even much lower modes when the neutrino heating time is slower (Kifonidis *et al.* 2006). In 3D modeling of a Type II progenitor, Meakin and Arnett (2007a,b) find that turbulent convection provides density perturbations at the oxygen/carbon interface that include structures in the rage of $m_0 \sim$ 24-48. If these predictions are correct, then asymptotic fast-phase SN instability growth will be dependent on the initial

conditions. Consequently, it is important to understand the spectral structure of the initial perturbations, as it likely determines the late-time structure of the mixing zone.

8. SPIKE MODELING AT HIGH ATWOOD NUMBER

For spikes, the drag term tends to zero and the terminal velocity diverges as the Atwood number approaches unity. Consequently, spikes at high Atwood number can require a long time to reach their terminal velocity, and the terminal velocity model will overestimate their growth. Early on, and as long as the drag term in the BD equation is small compared to the buoyancy term, we can use the free-fall instability velocity of equation (10). By equating the free-fall velocity $u_{ff} = Agt$ to the terminal velocity, we can estimate that the free-fall model is valid as long as

$$\frac{h_s}{\lambda} < \frac{1}{C_s}\frac{A^2}{1-A} \tag{23a}$$

or

$$m < \frac{2\pi}{C_s}\frac{A^2}{1-A}\frac{r}{h_s}. \tag{23b}$$

As shown in Fig. 9 where these expressions are plotted as functions of the post-shock density ratio, for sufficiently low mode spikes at small η^* the free-fall model is valid throughout the fast-growth phase.

Including the free-fall instability velocity equation (10) in the integrand of equation (7) for the modified amplitude, we find

$$H(t) = h^* + u_{i0}\int_{t_0}^{t} dt e^{-\int_{t_0}^{t'}\omega(t'')dt''} A\left[k_0 a_0 + \frac{1+\eta^*}{1+\eta^* C_a}\left(1-\frac{u_i(t')}{u_{i0}}\right)\right] \tag{24a}$$

$$\equiv H_0 + H_{RM} + H_{RT}\,. \tag{24b}$$

In addition to the initial amplitude term, there are separate contributions from RM and RT:

$$H_{RM}(t) = k_0 a_0 u_{i0}\int_{t_0}^{t} dt A e^{-\int_{t_0}^{t'}\omega(t'')dt''} \tag{25a}$$

$$H_{RT}(t) = u_{i0}\int_{t_0}^{t} dt e^{-\int_{t_0}^{t'}\omega(t'')dt''} A\frac{1+\eta^*}{1+\eta^* C_a}\left(1-\frac{u_i(t')}{u_{i0}}\right) \tag{25b}$$

The RM term is the standard impulsive model, linear in the initial k_0, modified by decompression stretching. The free-fall RT term is independent of the initial perturbation. In the free-fall approximation, the growth contribution due to RM exceeds the RT term a long as

$$k_0 a_0 > \frac{1+\eta^*}{1+\eta^* C_a}\left(1-\frac{u_i(t)}{u_{i0}}\right) \approx 1-\frac{u_i(t)}{u_{i0}}. \tag{26}$$

Thus RM always dominates initially and continues to be significant throughout the fast-growth phase if the initial amplitude is large ($k_0 a_0 \sim 1$). The RM impulsive model is a linear one, however, and so cannot be relied upon to give highly accurate predictions in the large-amplitude regime. Once perturbations become deeply nonlinear, we can no longer make conclusions about the relative importance of RT and RM based on the free-fall analysis.

Based on the $\eta = 0.01$ 1D simulation and neglecting the density gradient in the 1D flow ahead of the interface, the model predicts fast-phase growth given by

$$\frac{h_{\exp,f}}{r_f} = 0.86\frac{k_0 h^*}{m} = \frac{1}{42mA}\frac{2}{1+h_0/h^*}\frac{h_{RM,f}}{r_f} \tag{27a}$$

$$\frac{h_{RM,f}}{r_f} = 36.3Ak_0a_0 = 26.0k_0a_0 \tag{27b}$$

$$\frac{h_{RT,f}}{r_f} = 26.1A = 18.7, \tag{27c}$$

with a significant or dominant RM component relative to RT for $k_0 a_0 \geq 0.72$ (10% of the total for $k_0 a_0 = 0.07$). In general, the ratio of fast-phase RM to RT growth is given by

$$\frac{h_{RM,f}}{h_{RT,f}} = 1.4k_0a_0. \tag{28}$$

By construction, the free-fall model always predicts that spikes run well ahead of the shock during the fast-growth phase. In reality, the density gradient

typically results in significant drag before this occurs. As we shall see, where the post-shock density gradient ahead of the interface is insufficient to decelerate the spikes, their growth is instead limited by the upstream (in the shock frame) flow.

9. FREE-FALL MODEL IMPLICATIONS FOR TYPE Ia SUPERNOVAE

Chandra x-ray images of the Tycho SN remnant show striking instability growth. The measured power spectrum of the mixing zone is fit with a power-law power spectrum with peak at about mode 6 and an apparent local spectral peak at about mode 30 (Warren *et al.* 2005). Instability-driven spikes are observed at the forward shock, which is evidently strongly perturbed by their presence. SN remnant simulations predict significant separation between the shock and interface (Warren *et al.* 2005 and references therein) even when Rayleigh-Taylor effects are included (Dwarkadas 2000; Wang and Chevalier 2001).

However, it may yet be that hydrodynamic instabilities alone can explain the proximity of the spikes to the forward shock. Multi-dimensional simulations that predict greater spacing between the shock and interface are initialized with 1D input from explosion simulations or ejecta models. Since this initialization takes place after the forward shock has already passed into the ambient medium, it neglects any vorticity deposition at the interface due to the passing shock (ie the

RM component) that should be present in detonation models. If there are large-amplitude initial perturbations on either the interface or the shock front then this RM component would be a significant omission in the post-shock spike growth. Indeed, the observed structure of Tycho's interface and perturbed shock front is reminiscent of large amplitude RM observed in high-Mach-number laser-driven experiments [see, for example, our Fig. 10 adapted from Glendinning *et al.* (2003)].

The requirement for such shock proximity can be easily estimated for the planar shock case (Rikanati *et al.* 2003). The instability speed in the impulsive model is

$$u_{RM} = ka_0 A u_{i0}. \tag{29}$$

In the strong shock limit, the interface speed u_{i0} is related to the steady shock speed v_{i0} by

$$u_{i0} = \frac{2}{\gamma + 1} v_{i0}, \tag{30}$$

so the shock speed in the rest frame of the interface is

$$v_{i0} - u_{i0} = \frac{\gamma - 1}{2} u_{i0}. \tag{31}$$

Within the impulsive model, then, the spikes are predicted to overtake the shock if

$$ka_0 > \frac{\gamma - 1}{2A} \tag{32}$$

This condition can be satisfied either by large initial amplitude (large ka_0) or high compressibility (adiabatic index γ close to unity). With $\gamma = 5/3$ and $A = 1$, the condition for shock proximity is $ka_0 > 1/3$ ($ka_0 > 0.2$ for $\gamma = 1.4$ and $ka_0 > 1/6$ for $\gamma = 4/3$).

Log density plots from a 2D RAPTOR simulation of a spherical blast-wave-driven interface with $\gamma = 1.4$ and $kh_0 = 0.20$ ($ka_0 = 0.16$) are shown in Fig. 11. As predicted by the impulsive model for planar steady-shock RM, the spikes in this spherical blast-wave driven system grow up to and perturb the shock front, yielding structure that is reminiscent of the Tycho observations. Note that kh_0 here is comparable (actually slightly smaller) than that specified for the simulation shown in Fig. 3, but the presence of large-amplitude low modes in this case means that spikes extend further out in radius while remaining only marginally nonlinear. Consequently, we expect to find BWI shock proximity more readily observable when low modes are present in the initial conditions.

Figure 12 shows log density plots from a series of simulations with initial kh_0 varying from zero (in which perturbations are seeded only by numerics) up to unity. From this series, it appears that the threshold ka_0 for strong shock proximity is consistent with the prediction from the impulsive model for planar steady-shock RM. Figure 13 shows that the two main factors affecting shock proximity, initial amplitude and compressibility, can be traded off against each other while preserving the same degree of shock proximity.

Warren *et al.* (2005) report observed power spectra for both the interface and shock perturbations of the Tycho remnant that peak at mode six and exhibit a power-law decay ($\sim k^{-n}$) with $n \approx 1.5$ for the interface and $n \approx 2.2$ for the shock. The forward shock and contact discontinuity exhibit the same power at low modes, but there is an order of magnitude more power at the contact discontinuity at high mode numbers. This is qualitatively consistent with having the interface spectrum imprinted on the shock front at early time since the shock perturbations decay faster at higher wavenumber (D'yakov 1954; Landau and Lifshitz 1987). For strong shocks, we find that the dispersion relation for mode-ℓ shock perturbations is satisfied by an exponential decay rate of

$$\Gamma_\ell = \frac{\gamma-1}{\gamma+1} k v_s = \frac{\gamma-1}{\gamma+1} \frac{v_s}{R_s} \ell . \tag{33}$$

If we approximate the shock trajectory with spherical Taylor-Sedov scaling, then we have

$$\Gamma_\ell t = \frac{2}{5} \frac{\gamma-1}{\gamma+1} \ell \tag{34}$$

$$= \ell/10 \text{ for } \gamma = 5/3 \text{ and } \ell/15 \text{ for } \gamma = 1.4.$$

Allowing for the effect of divergence on the wavenumber, the evolution of shock perturbations that are decoupled from the piston (ie interface perturbations) is governed by

$$\frac{da_\ell}{dt} = -\frac{\gamma-1}{\gamma+1} \frac{v_s}{R_s} a_\ell . \tag{35}$$

For $v_s = \beta \cdot R_s / t$, this gives

$$a_\ell = a_{\ell 0}\left(\frac{R_{\ell 0}}{R_s}\right)^{\frac{\gamma-1}{\gamma+1}\ell} \tag{36}$$

independent of β, where $a_{\ell 0}$ and $R_{\ell 0}$ are the amplitude and shock radius at which the mode-ℓ shock perturbation is decoupled from the interface perturbation. Because different modes decouple from the shock at different radii, it is difficult to obtain a quantitative prediction of the shock front spectrum as a function of radius from equation (36). However, it does illustrate the faster decay of higher modes.

Delayed detonation offers a potential source of large-initial-amplitude low-mode RM. Even multi-spot ignition models in Type Ia explosion simulations produce very low modes via RT-unstable deflagration (for example Ropke *et al.* 2006). These modes exist in the form of large-scale ash bubbles surrounded by higher-density unburned fuel. In the delayed detonation picture, a supersonic detonation then consumes the remaining fuel. As it propagates around the ash bubbles, this supported shock must also send lower-velocity unsupported shocks into the bubbles, resulting in a highly perturbed shock emerging from the outer extent of the deflagration region. Indeed, such a highly structured shock is evident in 3D delayed-detonation simulations (Fig. 1 of Gamezo *et al.* 2004). If the deflagration region extends far enough out that the shock does not have time to symmetrize before reaching the surface of the star, then we would have precisely

the kind of large-amplitude low-mode RM BWI component that should produce shock proximity at the present Tycho epoch.

In that case, the dominant low modes observed in the Tycho remnant would result directly from the initial perturbations rather than an inverse cascade from smaller scales. Such a direct correlation between the asymptotic structure and the initial conditions would mean that structure observed now contains information about the combustion process. For example, the shock structure in the Gamezo *et al.* (2004) simulations might exhibit a spectrum comparable to that observed in present-day Tycho observations, while an off-center detonation not preceded by a deflagration stage might seed a dominant $\ell = 1$ mode. If cosmic-ray acceleration and other scenarios are deemed insufficient to produce the observed degree of shock proximity, then combustion models that do not include a detonation phase might be ruled out.

10. FREE-FALL MODEL IMPLICATIONS FOR TYPE II SUPERNOVAE

Enhanced growth of perturbation spikes relative to the forward shock due to the RM component appears to play an important role in Type II explosion simulations of Kifonidis *et al.* (2006). In these calculations, a longer neutrino heating time results in vigorous convection in the star's core. This in turn yields

kinks in the forward shock that deposit vorticity as they are transmitted through the inner interfaces. Spikes associated with these large-amplitude low-mode perturbations grow up to the shock, allowing core material to mix through to the hydrogen shell without deceleration by the post-shock helium shell. Such deceleration in the same group's earlier calculations reduced heavy element velocities to values inconsistent with observations (Kifonidis *et al.* 2003). With the slower neutrino heating and consequent large-amplitude RM, the calculated velocities agree with the data.

11. ROLE OF HIGH-ENERGY-DENSITY LABORATORY ASTROPHYSICS

Euler scaling and the unified nature of the blast-wave-driven interface problem mean that the hydrodynamics at work in the supernova can be scaled down and studied in the laboratory. Laser-driven laboratory experiments are routinely used to study shock- and blast-wave-driven instabilities, and Euler scaling has been applied to make connections to astrophysical systems such as supernovae (Ryutov *et al.* 1999; Remington *et al.* 2006 and references therein).

In ongoing planar experiments at the OMEGA laser facility (Soures 1996) at the University of Rochester's Laboratory for Laser Energetics, the laser is used to drive a high-Mach-number planar blast wave into one end of a cylindrical

target (Drake *et al*., 2002; Robey *et al*. 2003; Miles *et al*. 2004). The target consists of a higher-density plastic section and a lower-density foam section in contact along a perturbed interface. X-ray radiography through the side of the target is used to produce images of the developing instability analogous to those obtained in the RM experiment of Fig. 10. The incident blast wave in these experiments is sufficient to drive the instability deep into the nonlinear regime.

Because analogous divergent blast-wave-driven experiments would require much more drive energy, they cannot be realized on the OMEGA laser facility. On the other hand the National Ignition Facility (NIF) (Campbell 1991), now nearing completion at Lawrence Livermore National Laboratory, will offer the possibility to conduct a truly SN-relevant divergent experiment. The axially symmetric target could notionally consist of concentric titanium, heavy-foam, and light-foam shells that are mass-scaled surrogates for the metal, helium, and hydrogen shells in a Type II SN progenitor (see Fig. 14), with perturbations machined onto one or both of the surrogate Si/O and He/H interfaces. A nanosecond-scale laser pulse would be used to drive a divergent blast wave into the target, and the evolving structure could be imaged at times exceeding 100 ns. This platform would allow investigation of appropriate multi-interface interactions including the deceleration of fast inner spikes by the outer-layer shell, divergence effects, sensitivity to initial perturbations, 3D vs 2D and turbulent vs. non-turbulent instability evolution, and code validation. For example, Fig. 15

shows predictions from a pair of CALE simulations of a notional experiment to investigate the effect of large-amplitude low modes on mixing of surrogate core material out into the surrogate hydrogen shell.

A Type Ia-relevant experiment would be very similar but would include a single interface that could include perturbations of various initial amplitudes to investigate shock proximity effects. Various ambient-medium surrogates could be used to investigate compressibility effects on the shock-interface standoff.

10. CONCLUSIONS AND FUTURE DIRECTIONS

In summary, the divergent blast-wave-driven interface is a fundamental hydro instability problem that is particularly relevant to mixing in SNe. The existence of unified solutions at high Mach number and small density ratio suggests that general conclusions can be drawn about the likely asymptotic structure of the mixing zone. Insight into these conclusions can be attained by application of simple buoyancy-drag and bubble merger models modified to include the effects of divergence and decompression. In general, these effects preclude the true self-similar growth of classical RT, but can be incorporated into a quasi-self-similar growth picture. Where the unified solution to the 1D problem applies, multi-dimensional instability growth is not predicted to be strictly unified.

Loss of memory of initial conditions can occur in the quasi-self-similar model, but high initial mode numbers are required for this to happen during the fast-growth phase. Despite the high-mode-number requirement for true loss of memory of initial conditions and the lack of strictly unified perturbation growth, the late-time asymptotic structure of the mixing zone is only weakly dependent on the initial conditions over a wide range of density ratios and initial perturbations. Still, since very high modes are not dominant in the initial conditions predicted for Type II SNe, their late-time instability growth is likely influenced by details of the initial conditions.

Where dominant low-modes are observed (up to about mode ten), they result from the initial perturbations rather than an inverse cascade from smaller scales. This means that the interface structure observed now in the Tycho remnant contains direct information about the combustion process.

Large-amplitude initial conditions yield an RM contribution that is significant or dominant relative to RT. The RM contribution will always be present where interface and transmitted shock are misaligned, whether due to pre-transmission perturbations on the interface or the shock front. For sufficiently large-amplitude perturbations, we expect shock proximity to the growing spikes throughout the fast-growth phase. In the BWI system, the shock proximity effect can produce shock-interface structure that closely resembles that observed in the

Tycho remnant. Initial conditions required to produce such structure might naturally arise following a deflagration to detonation transition.

In the future, we intend to run 3D simulations of the BWI system for comparison of 2D vs. 3D effects. Relative to the 2D calculations presented here, we expect faster spike growth and a further relaxed shock proximity requirement. The inverse cascade to larger scales should proceed more slowly in 3D than in 2D, and the mixing zone will exhibit finer mixing and more small-scale turbulent structure like that apparent in the Tycho remant but not the simulation in Fig. 12.

Finally, Euler scaling and the unified nature of the BWI problem enable scaled laboratory experiments that are relevant to supernova instability hydrodynamics. Consequently, laser-driven laboratory experiments might be used to help resolve some of the outstanding questions in supernova explosion hydrodynamics.

ACKNOWLEDGEMENTS

This work was performed under the auspices of the U.S. Department of Energy by Lawrence Livermore National Laboratory in part under Contract W-7405-Eng-48 and in part under Contract DE-AC52-07NA27344.

REFERENCES

Alon, U., Hecht, J, Mukamel, D, and Shvarts, D. 1994, *Phys. Rev. Lett.*, **72**(18), 2867.

Arnett, W. D. 1969, *Astrophys. Space Sci*., **5**, 180.

Barton, R. T. 1985, *Numerical Astrophysics* (Jones and Bartlett, Boston).

Blinnikov, S., Lundqvist, P., Bartunov, O., *et al.* 2000, *Ap. J.*, **532**, 1132.

Blondin, J. and Ellison, D. 2001, *Ap. J*., **560**, 244.

Bravo, E. and Garcia-Senz, D. 2006, *Ap.J.,* **642**, L157.

Campbell, E. M. 1991, *Laser Part. Beams*, **9**(2), 209.

Chevalier, R. A. 1976, *Ap.J.*, **207**, 872.

Chevalier, R. A. 1977, *ARA&A*, **15**, 175.

Chevalier, R. A., Blondin, J. M., and Emmering, R. T. 1992, *Ap. J*., **392**, 118.

Truelove and McKee 1999.

Davies, R. M. and Taylor, G. I. 1950, *Proc. R. Soc. London Ser. A,* **200**, 375.

Davies, B. & Tout, C. A., (NATO ASI Ser. C, Vol. 477; Dordrecht: Kluwer), 307.

Decourchelle, A., Ellison, D., and Ballet, J. 2000, *Ap. J*., **543**, L57.

Dimonte, G., and Schneider, M. 1996, *Phys. Rev. E*, **54**, 3740.

Drake, R. P., Robey, H. F., Hurricane, O. A., *et al*. 2002, *Ap*. *J*., **564**, 896.

Dwarkadas, V. V. 2000, *Ap. J.*, **541**, 418.

D'yakov, S. P. 1954, *Zh. Eksp. Teor. Fiz*., **27**, 288.

Falk, S. W., and Arnett, W. D. 1973, *Ap. J. (Letters)*, **180**, L65.

Fryxell, B. A., Muller, E., and Arnett, W. D. 1991, *Ap. J.*, **367**, 619.

Gamezo, V. N., Khokhlov, A. M., and Oran, E. S. 2004, *Ap. J.*, **623**, 337.

Glendinning, S. G., Bolstad, J., Braun, D. G., *et al.* 2003, *Phys. Plasmas,* **10**(5), 1931.

Glimm, J., and Li, X. L. 1988, *Phys. Fluids*, **31**(8), 2077.

Gull, S. F. 1973, *MNRAS*, **161**, 47.

Hanson, J. C. V., Rosen, P. A., Goldsack, *et al.* 1990, Laser Part. Beams **8**, 51.

Hillebrandt, W. and Niemeyer, J. 2000, *ARA&A*, **38**, 191.

Howell, L. H., and J.A. Greenough 2003, *J. Comp. Phys*., **184**, 53.

Hoyle, F. and Fowler, W. 1960, *Ap.J*., **132**, 565.

Hurricane, O. A. 2005, *Phys. Fluids* **17**, 058103.

Ivanova, L. N., Imshennik, V. S., and Chechetkin, V. M. 1974, *Astrophys. Space Sci*., **31**, 497.

Jun, B.-I., Jones, T. W., and Norman, M. L. 1996, *Ap. J.*, **468**, L59.

Khokhlov, A. M. 1991, *Astr. Ap.*, **245**, 114.

Khokhlov, A. M. 1995, *Ap. J.*, **449**, 695.

Kifonidis, K., Plewa, T., Janka, H.-Th., and Muller, E. 2003, *Astr. Ap.*, **408**, 621.

Kifonidis, K., Plewa, T., Scheck, L., Janka, H.-Th., and Muller, E. 2006, *Astr. Ap.*, **453**, 661.

Landau, L. D. and Lifshitz, E. M. 1987, *Fluid Mechanics* (2nd ed.; Oxford: Pergamon).

Layzer, D. 1955, *Ap. J.,* **122**, 1.

McKee, C. F. and Truelove, J. K., 1995, *Phys. Rep.*, **256**, 157.

Meakin, C. A. and Arnett, D. 2007a, *Ap. J.*, **665**, 690.

Meakin, C. A. and Arnett, D. 2007b, *Ap. J.*, **667**, 448.

Meshkov, EE. 1969, *Izv. AN SSSR Mekhanika Zhidkosti I Gaza,* **4**(5), 151.

Meyer, K. A. and Blewett, P. J. 1972, *Phys. Fluids* **15**(5), 753.

Miles, A. R., Braun, D. G., Edwards, M. J., *et al.* 2004, *Phys. Plasmas,* **11**(7), 3631.

Miles, A. R. 2004, *Phys. Plasmas*, **11**(11), 5140.

Mitchell, R. C., Baron, E., Branch, D. 2001, *et at.*, *Ap. J.*, **556**, 979.

Muller, E., Fryxell., B. A., and Arnett, W. D. 1991, *Astr. Ap.*, **251**, 505.

Nomoto, K., Sugimoto, D., and Neo, S. 1976, *Astrophys. Space Sci*., **39**, L37.

Nugent, P., Baron, E., Branch, D., Fischer, A., and Hauschildt, P. 1997, *Ap.J*., **485**, 812.

Oron, D., Arazi, L., Kartoon, D., *et al.* 2001, *Phys. Plasmas*, **8**(6), 2883.

Ott, E. 1972, *Phys. Rev. Lett.*, **29**, 1429.

Plewa, T., Calder, A., and Lamb, D. 2004, *Ap.J*., **612**, L37.

Richtmyer, R. D. 1960, *Commun. Pure Appl. Math.,* **13**, 297.

Rayleigh 1899, *Scientific Papers* (University press, Cambridge).

Remington, B. A., Drake, R. P., and Ryutov, D. D. 2006, *Rev. Mod. Phys.*, **78**, 755.

Rikanati, A., Oron, D., Sadot, O., and Shvarts, S. 2003, *Phys. Rev. E*, **67**, 026307.

Robey, H. F., Zhou, Y., Buckingham, A. C., *et al.* 2003, *Phys. Plasmas,* **10**, 614.

Ropke, F. K., Hillebrandt, W., Niemeyer, J. C., and Woosley, S. E., *Astr. Ap.*, **448**(1), 1.

Ryutov, D., Drake, R. P., Kane, Liang, J. E., Remington, B. A., and Wood-Vasey, W. M.

1999, *Ap. J.,* **518**, 821.

Sedov, L. I. 1946a, *Dokl. Akad. Nauk SSSR*, **42**, 17.

Sedov, L. I. 1946b, *Prikl. Mat. Mekh*., **10**, 241.

Sedov, L. I. 1959, *Similarity and Dimensionless Methods in Mechanics* (4^{th} ed.; New York: Academic).

Sedov, L. I. 1992, *Similarity and Dimensionless Methods in Mechanics* (10^{th} ed.; Boca Raton: CRC: Academic).

Sharp, K. I. 1984, *Physica D,* **12**, 3.

Shvarts, D., Alon, U., Ofer, D., McCrory, R. L., and Verdon, C. P. 1995, *Phys. Plasmas*, **2**, 2465.

Soures, J. M., McCrory, R. L., Verdon, C. P. 1996, *et al.*, *Phys. Plasmas*, **5**, 2108.

Taylor, G. I. 1950, *Proc. R. Soc. London*, *Ser. A*, **201**, 192.

Truelove, J. K. and McKee, C. F. 1999, *Ap. J. Sup. Ser.*, **120**,299.

Tueller, J., Barthelmy, S., Gehrels, *et al.* 1990, *Ap. J.,* **351**, L41.

Wang, C.-Y. and Chevalier, R., A. 2001, *Ap. J.*, **549**, 1119.

Warren, J. S., Hughes, J. P., Badenes, C., *et al.* 2005, *Ap. J.*, **634**, 376.

Wheeler, J. C. 1996, in Evolutionary Processes in Binary Stars, ed. R. A. M. J. Wijers, M.

Youngs, D. L. 1984, *Physica D*, **12**, 32.

Fig. 1.--Blast-wave instability (BWI) schematic: A blast wave is initiated at the center of a sphere of density ρ_1 located in an ambient fluid with density ρ_2. Perturbations on the surface of the sphere are driven unstable upon passage of the blast wave, and subsequently grow in amplitude under the combined effect of Richtmyer-Meshkov (RM), Rayleigh-Taylor (RT), and material decompression. The six dimensional parameters in the unperturbed problem are the drive pressure $P \propto E \propto T$, the piston radius r_p, the sphere radius r_0, the densities $\rho_1 \propto m_1$ and ρ_2, and the ambient pressure P_0. This number is reduced to four when the conditions $P/P_0 >> 1$ and $r_p/r_0 << 1$ are satisfied and to three when in addition $\eta << 1$.

Fig. 2.--Radius-time (r-t) diagram for a blast-wave driven interface with $P/P_0 = 10^9$, $r_0/r_p = 10$, and $\eta = 0.01$. The equal mass radius r_m, which is the point at which the interface has swept up a mass of low density material equal to the mass of the

denser fluid, is the governing length scale. The evolution of the problem is divided into three phases: an early-time ejecta-dominated (ED) phase, an intermediate phase, and the late-time Taylor-Sedov (TS) phase.

Fig. 3.--Log density plots from a two dimensional RAPTOR simulation illustrate BWI perturbation growth. Dimensionless time and interface radius (see text) are shown for each image. In this case $P/P_0 = 10^7$, $r_0/r_p = 2.25$, and , and $\eta = 0.01$. The incident blast wave crosses the interface at $\tau \approx 0.2$ between (a) and (b). The reverse shock forms and begins to propagate back towards the center in (c), where it converges in (d). Multimode perturbations seeded on the interface grow into outward-going spikes of material 1 and inward "rising" bubbles of material 2. In (e), the reflected reverse shock returns to the developing mixing zone, which is reshocked in (f). This second shock exits the mixing zone in (g) on its way to overtake the main shock, having set a very complicated initial condition for the ensuing TS phase.

Fig. 4.--Scaled radius vs time plots for blast-wave-driven interfaces with various density ratios. In each case $P/P_0 = 10^9$ and $r_0/r_p = 10$. Radius and time are in each case scaled by the equal mass radius and time defined in the text. At low density ratio, a unified solution exists and the scaled plots are nearly identical.

Fig. 5.--Log density images from a pair of RAPTOR simulations with different drive pressures illustrate the drive-energy independence of the instability growth for identical initial perturbation spectra and radii. With the drive pressure lower by a factor of 100, the characteristic time is a factor of 10 longer but the interface structure is qualitatively the same at the same scaled time. In each case $P/P_0 = 10^9$ and $r_0/r_p = 2.25$ and we are comparing at $r_i/r_m = 1.5$.

Fig. 6.--Scaled (a) decompression factor, (b) decompression factor scaled by r_0/r_m, (c) RT growth function, (d) growth function scaled by $(r_0/r_m)^2$, (e) stretch function scaled by $(r_0/r_m)^2$, and (f) ratio of RT growth function to stretch function. All are shown for three different density ratios and two scaled piston radii. At low density ratio where the unified solution to the 1D blast-wave-driven interface problem is valid, the decompression factor, RT growth function, and stretch function are not unified, but can be made so by scaling by powers of r_0/r_p. The growth and stretch functions require the same scale factor. Therefore their ratio, which is proportional to the nonlinear single-mode growth predicted by the terminal-velocity buoyancy-drag model for high mode numbers, is also unified.

Fig. 7. Buoyancy-drag and QSS model inputs and predictions for a system with $P/P_0 = 10^9$, $r_0/r_p = 10$, $\eta = 0.01$, and characteristic $m_0 = 160$, with inputs taken from a 1D simulation. All are plotted against the scaled interface radius: (a)

Interface velocity and velocity gradient at the interface position, (b) RT growth function and QSS self-similarity function, (c) mode number with scaled amplitude as fiducial, and (d) bubble amplitude (nonlinear single-mode as well as QSS multimode) and interface acceleration. In (c) and (d), blue triangles denote results from a 2D RAPTOR simulation. Nonlinear single-mode growth is used until the bubble-merger threshold $h = l/\sigma$ is reached. Up to the equal-mass radius ($\xi = 1$), the velocity gradient is negative and the interface is in compression. During this time and once bubble merger is initiated, we fix the QSS self-similarity parameter to unity. Bubble merger and amplitude growth are halted when the reflected reverse shock reaches the mixing zone.

Fig. 8.--Asymptotic fast-phase (a) scaled bubble amplitude, (b) mode number, and (c) QSS function from the quasi-self-similar growth model vs initial mode number m_0. In the amplitude plot, dashed lines denote the growth predicted for nonlinear single-mode perturbations. At high initial mode number, the interface structure loses its dependence on m_0, signifying that memory of the initial conditions has been lost. When very low, the density ratio has only a weak effect on the asymptotic interface structure.

Fig. 9.--Range of validity of the freefall model for spikes at low density ratio: (a) limiting spike amplitude normalized to perturbation wavelength. (b) Limiting

mode number for the case of spike amplitude equal to interface radius. At low density ratio, the freefall model remains valid for sufficiently low mode-spikes throughout the fast-growth phase.

Fig. 10.--X-ray radiograph of a laser-driven planar RM experiment with large initial amplitude ($kh_0 = 0.92$, $\lambda = 150$ μm) [Adapted from Glendinning *et al.* 2003]. A Mach ~ 10 steady shock is incident on a perturbed plastic/foam interface. Due to the large initial amplitude, the RM spike growth speed is higher than the shock recession speed in the interface frame. Consequently, the spikes grow up to and perturb the shock front.

Fig. 11.--Large amplitude BWI exhibits shock proximity at the scaled Tycho SNR radius [(Forward shock radius)/(Reverse shock radius) ~ 0.7] and shock-interface structure that resembles *Chandra* x-ray data (Warren *et al.* 2005). The initial perturbation spectrum proscribed in the simulation is peaked at mode six with a power law decay to higher mode numbers.

Fig. 12.--Varying the degree of shock proximity by changing the initial amplitude in a series of RAPTOR BWI simulations. At small initial amplitude, the RM contribution to the fast-phase growth is also small and the shock front is smooth. At about the threshold predicted by the planar strong shock relations and

impulsive RM model ($ka_0 = 0.2$ for $\gamma = 1.4$), the spikes extend to and perturb the shock front.

Fig. 13.--Log density plots from a pair of RAPTOR BWI simulations in which the initial amplitude and fluid compressibility are traded off each other while preserving the degree of shock proximity predicted by the planar strong shock relations and impulsive RM model.

Fig. 14.--Notional divergent multi-interface Type II SN experiment for the National Ignition Facility laser. Titanium, heavy-foam, and light -oam shells are mass-scaled surrogates for the metal, helium, and hydrogen shells in the progenitor star. Consequently, the evolving structure is comparable to that observed in core-collapse simulations of Kifonidis *et al.* (2003).

Fig. 15.--Prediction for a pair of laser-drive NIF experiments designed to investigate the effect of having large-amplitude low modes in the initial conditions. In each case, the magenta insert shows the initial Ti inner shell. The lower half of each figure shows density, while the upper half is colored by material: Titanium (core surrogate) is aqua, heavy foam (helium surrogate) is green, and light foam (hydrogen surrogate) is blue. In (b), a large-amplitude mode six pre-imposed on the laser-irradiated surface results in a perturbed shock that

transmits that mode to the core/He interface surrogate. This results in enhanced mixing through the surrogate He/H mixing zone.

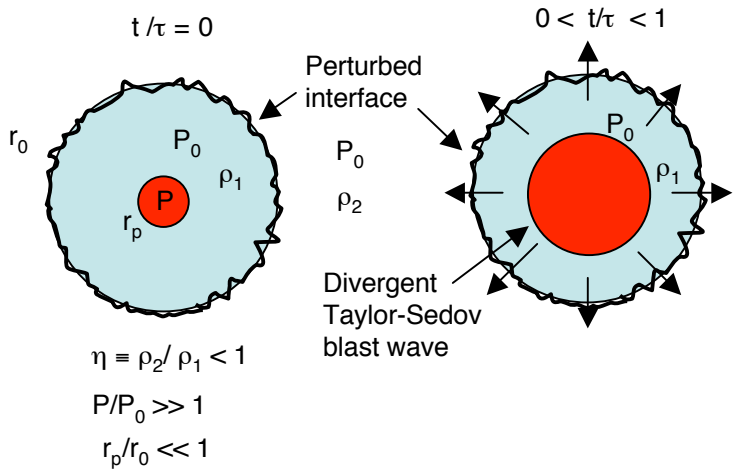

Fig. 1.--Blast-wave instability (BWI) schematic: A blast wave is initiated at the center of a sphere of density ρ_1 located in an ambient fluid with density ρ_2. Perturbations on the surface of the sphere are driven unstable upon passage of the blast wave, and subsequently grow in amplitude under the combined effect of Richtmyer-Meshkov (RM), Rayleigh-Taylor (RT), and material decompression. The six dimensional parameters in the unperturbed problem are the drive pressure $P \propto E \propto T$, the piston radius r_p, the sphere radius r_0, the densities $\rho_1 \propto m_1$ and ρ_2, and the ambient pressure P_0. This number is reduced to four when the conditions $P/P_0 >> 1$ and $r_p/r_0 << 1$ are satisfied and to three when in addition $\eta << 1$.

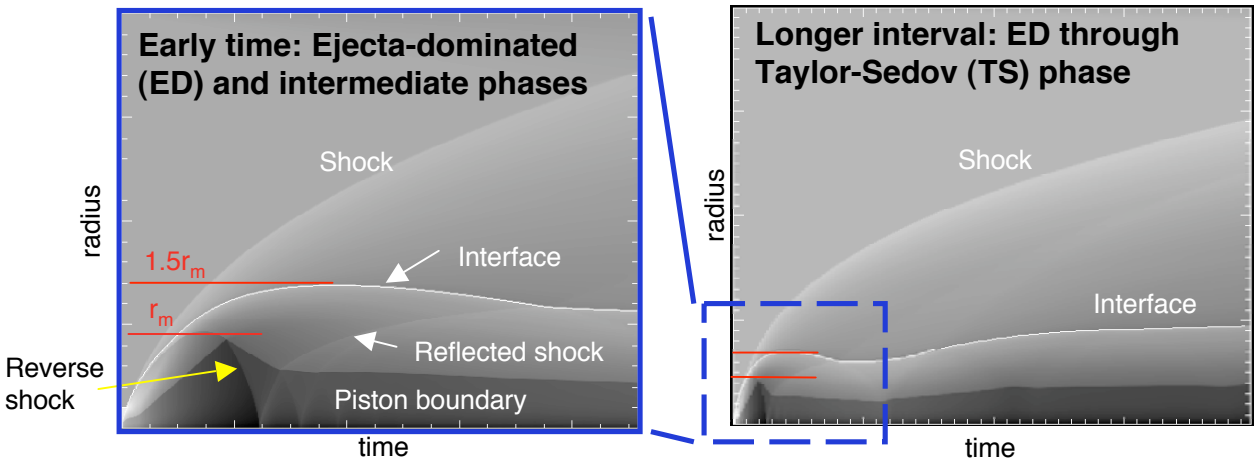

Fig. 2.--Radius-time (r-t) diagram for a blast-wave driven interface with $P/P_0 = 10^9$, $r_0/r_p = 10$, and $\eta = 0.01$. The equal mass radius r_m, which is the point at which the interface has swept up a mass of low density material equal to the mass of the denser fluid, is the governing length scale. The evolution of the problem is divided into three phases: an early-time ejecta-dominated (ED) phase, an intermediate phase, and the late-time Taylor-Sedov (TS) phase.

Fig. 3.--Log density plots from a two dimensional RAPTOR simulation illustrate BWI perturbation growth. Dimensionless time and interface radius (see text) are shown for each image. In this case $P/P_0 = 10^7$, $r_0/r_p = 2.25$, and , and $\eta = 0.01$. The incident blast wave crosses the interface at $\tau \approx 0.2$ between (a) and (b). The reverse shock forms and begins to propagate back towards the center in (c), where it converges in (d). Multimode perturbations seeded on the interface grow into outward-going spikes of material 1 and inward "rising" bubbles of material 2. In (e), the reflected reverse shock returns to the developing mixing zone, which is reshocked in (f). This second shock exits the mixing zone in (g) on its way to overtake the main shock, having set a very complicated initial condition for the ensuing TS phase.

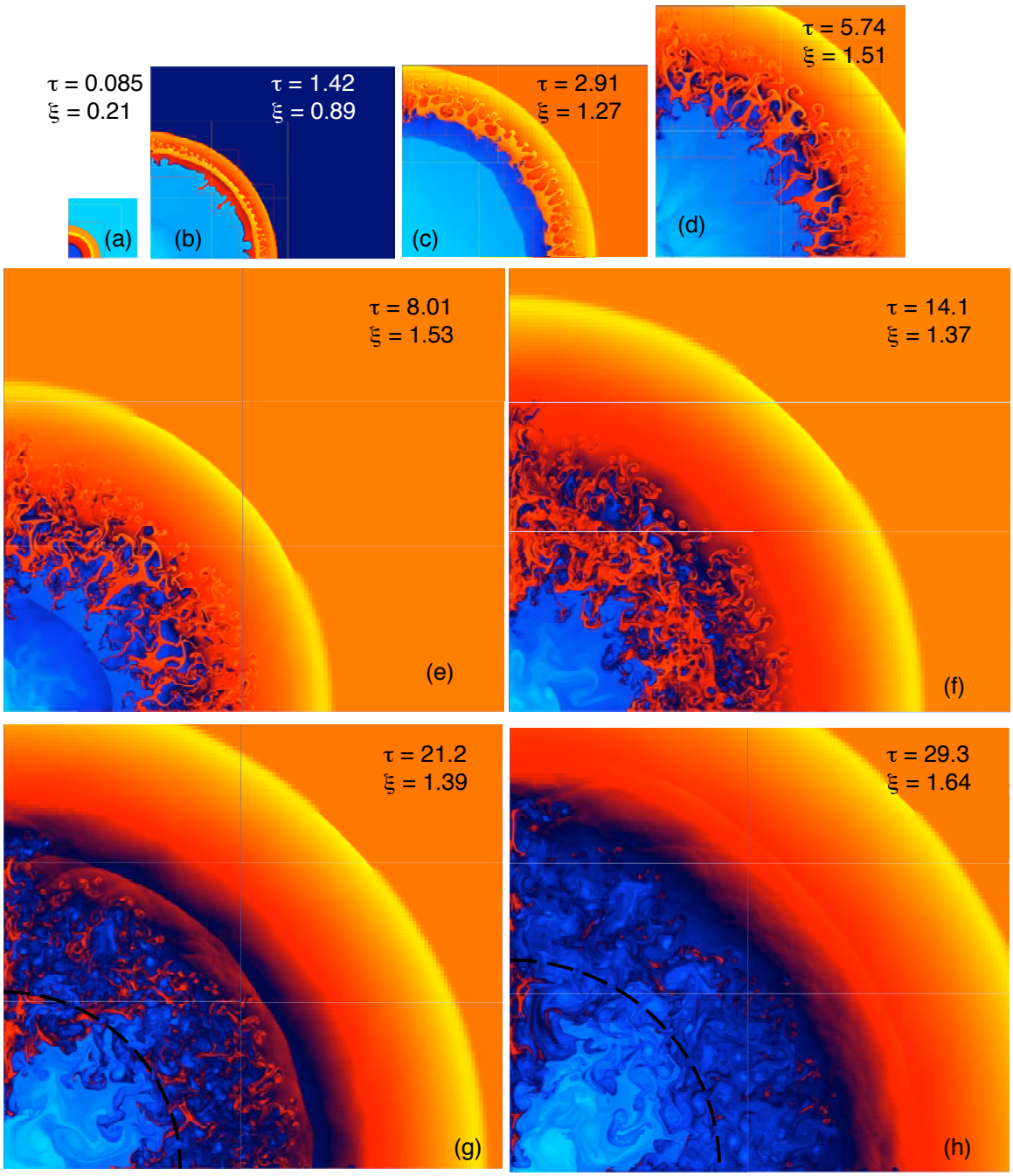

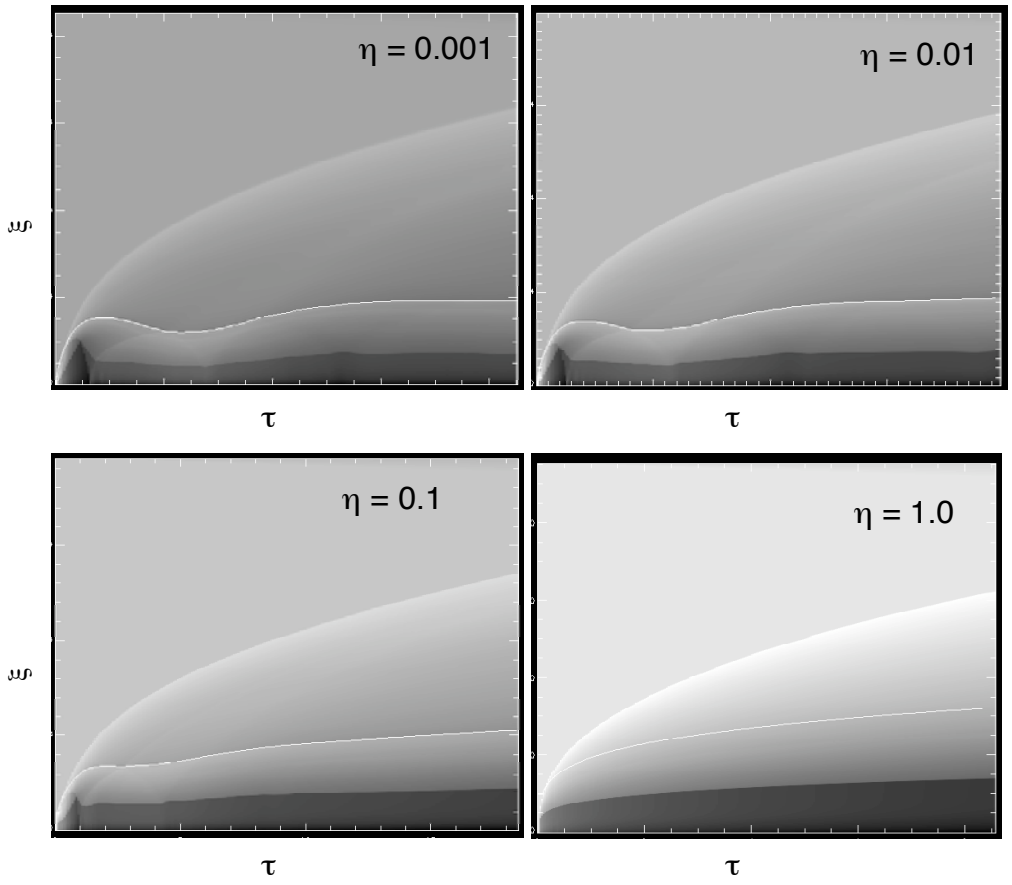

Fig. 4.--Scaled radius vs time plots for blast-wave-driven interfaces with various density ratios. In each case $P/P_0 = 10^9$ and $r_0/r_p = 10$. Radius and time are in each case scaled by the equal mass radius and time defined in the text. At low density ratio, a unified solution exists and the scaled plots are nearly identical.

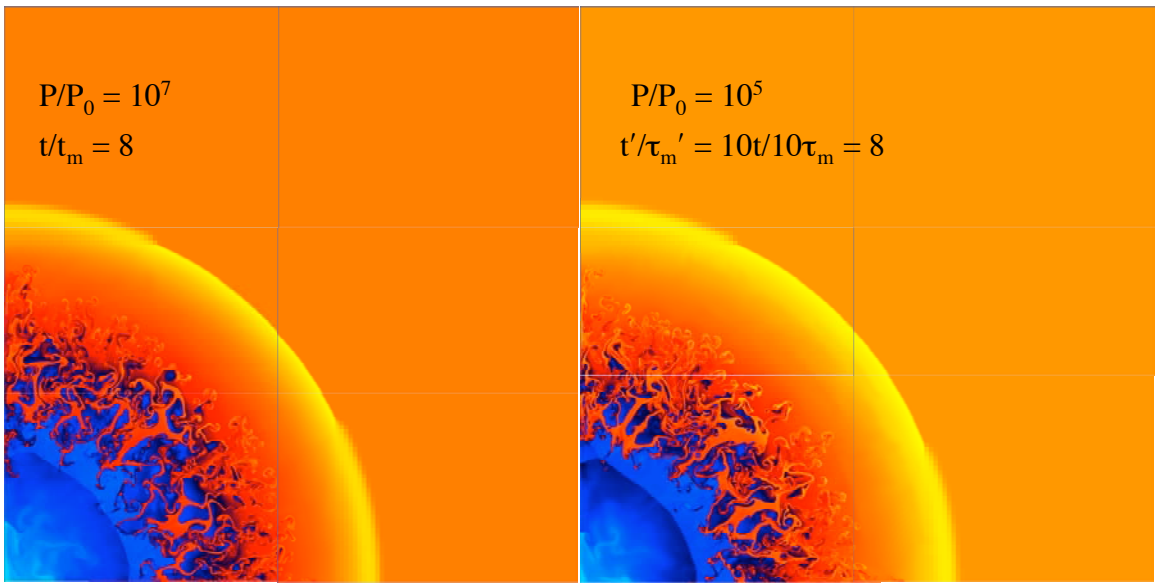

Fig. 5.--Log density images from a pair of RAPTOR simulations with different drive pressures illustrate the drive-energy independence of the instability growth for identical initial perturbation spectra and radii. With the drive pressure lower by a factor of 100, the characteristic time is a factor of 10 longer but the interface structure is qualitatively the same at the same scaled time. In each case $P/P_0 = 10^9$ and $r_0/r_p = 2.25$ and we are comparing at $r_i/r_m = 1.5$.

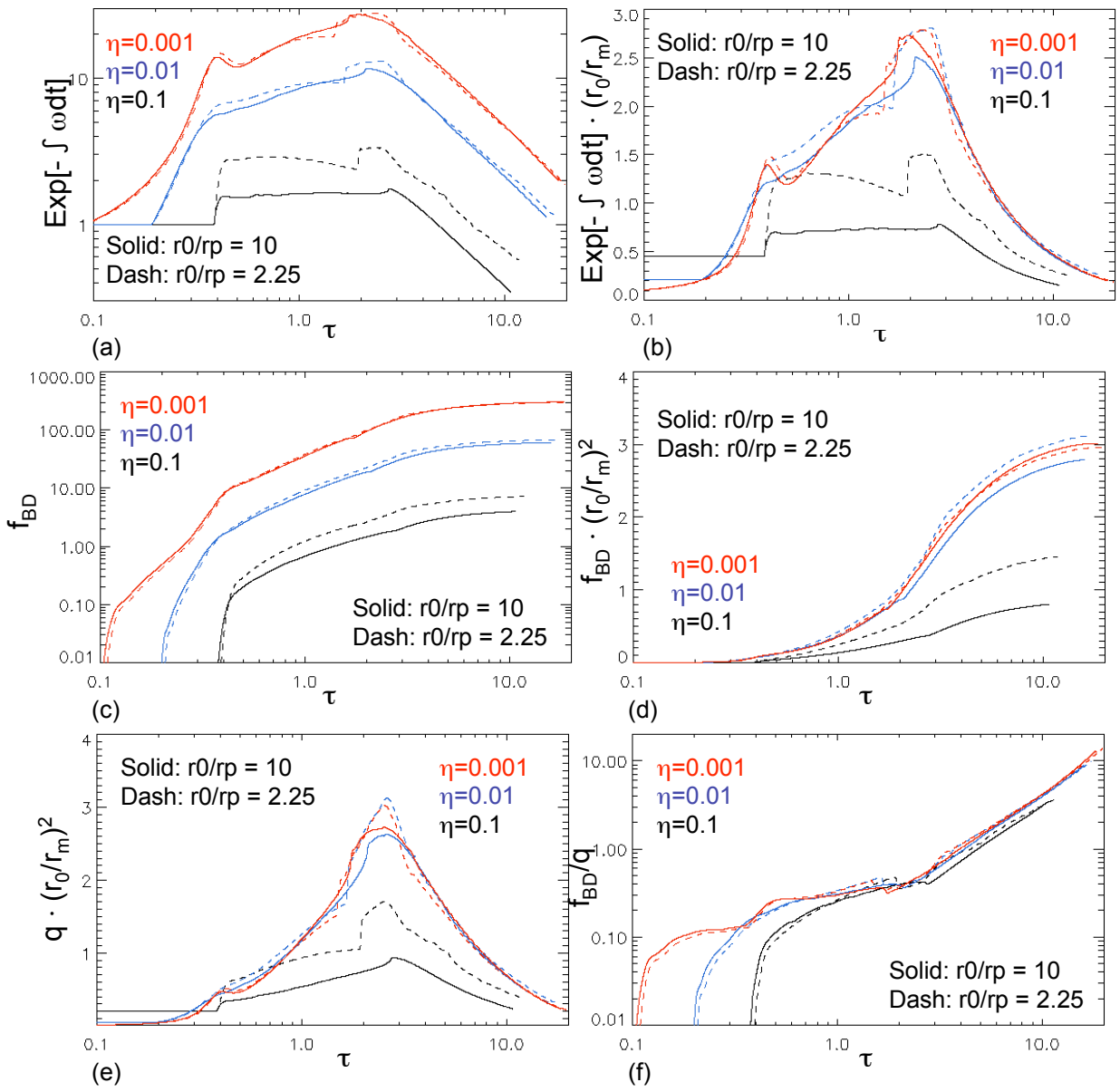

Fig. 6.--Scaled (a) decompression factor, (b) decompression factor scaled by r_0/r_m, (c) RT growth function, (d) growth function scaled by $(r_0/r_m)^2$, (e) stretch function scaled by $(r_0/r_m)^2$, and (f) ratio of RT growth function to stretch function. All are shown for three different density ratios and two scaled piston radii. At low density ratio where the unified solution to the 1D blast-wave-driven interface problem is valid, the decompression factor, RT growth function, and stretch function are not unified, but can be made so by scaling by powers of r_0/r_p. The growth and stretch functions require the same scale factor. Therefore their ratio, which is proportional to the nonlinear single-mode growth predicted by the terminal-velocity buoyancy-drag model for high mode numbers, is also unified.

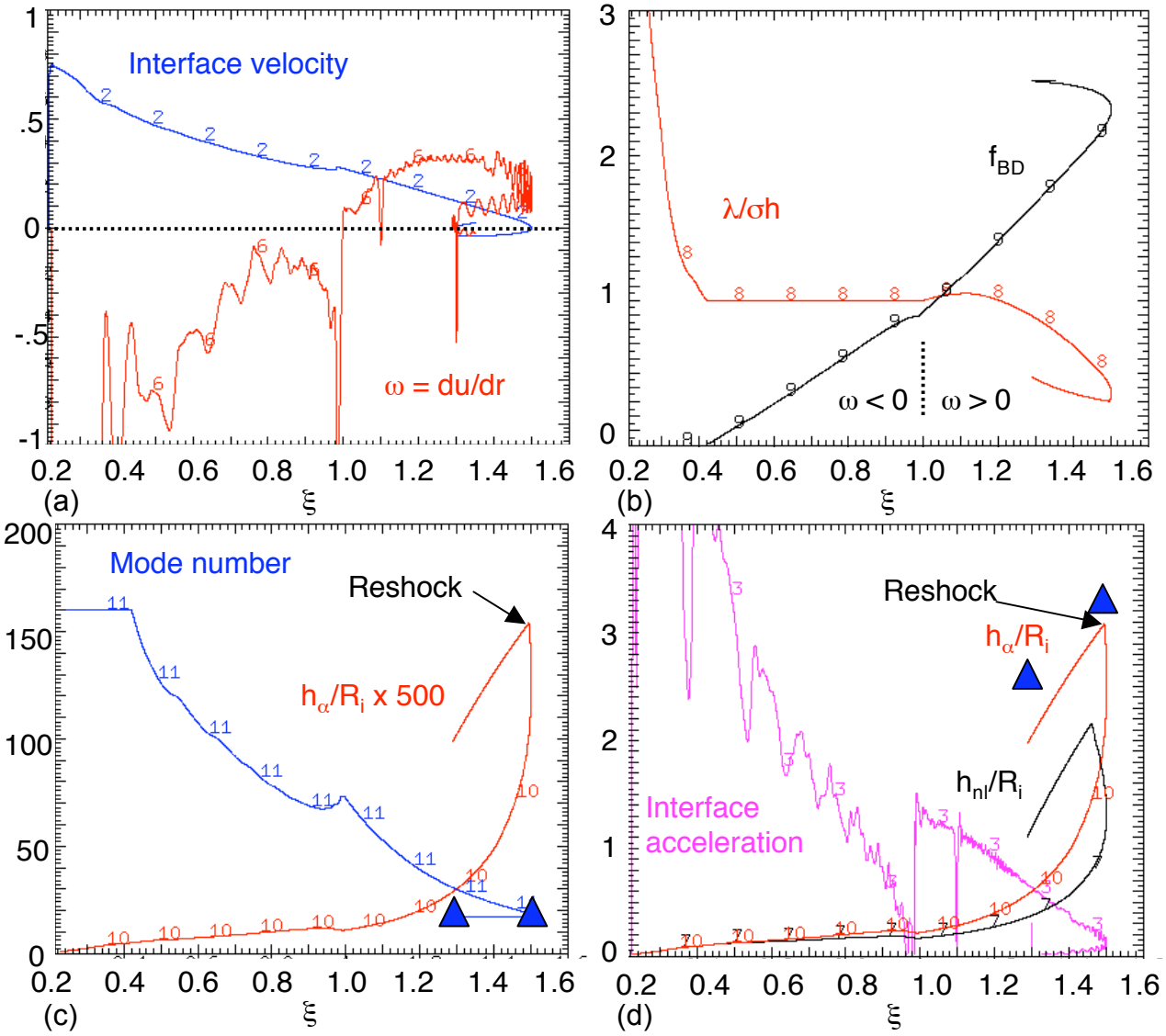

Fig. 7. Buoyancy-drag and QSS model inputs and predictions for a system with $P/P_0 = 10^9$, $r_0/r_p = 10$, $\eta = 0.01$, and characteristic $m_0 = 160$, with inputs taken from a 1D simulation. All are plotted against the scaled interface radius: (a) Interface velocity and velocity gradient at the interface position, (b) RT growth function and QSS self-similarity function, (c) mode number with scaled amplitude as fiducial, and (d) bubble amplitude (nonlinear single-mode as well as QSS multimode) and interface acceleration. In (c) and (d), blue triangles denote results from a 2D RAPTOR simulation. Nonlinear single-mode growth is used until the bubble-merger threshold $h = l/\sigma$ is reached. Up to the equal-mass radius ($\xi = 1$), the velocity gradient is negative and the interface is in compression. During this time and once bubble merger is initiated, we fix the QSS self-similarity parameter to unity. Bubble merger and amplitude growth are halted when the reflected reverse shock reaches the mixing zone.

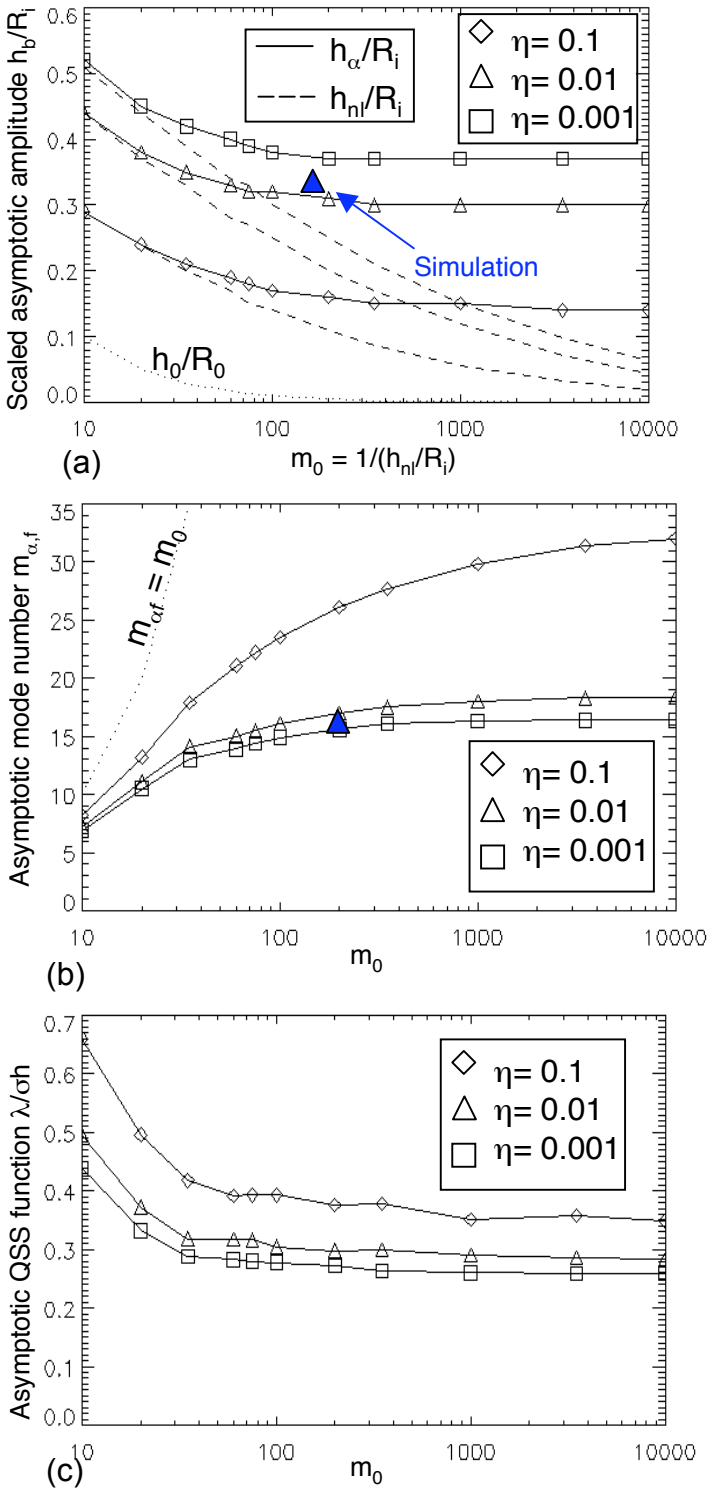

Fig. 8.--Asymptotic fast-phase (a) scaled bubble amplitude, (b) mode number, and (c) QSS function from the quasi-self-similar growth model vs initial mode number m_0. In the amplitude plot, dashed lines denote the growth predicted for nonlinear single-mode perturbations. At high initial mode number, the interface structure loses its dependence on m_0, signifying that memory of the initial conditions has been lost. When very low, the density ratio has only a weak effect on the asymptotic interface structure.

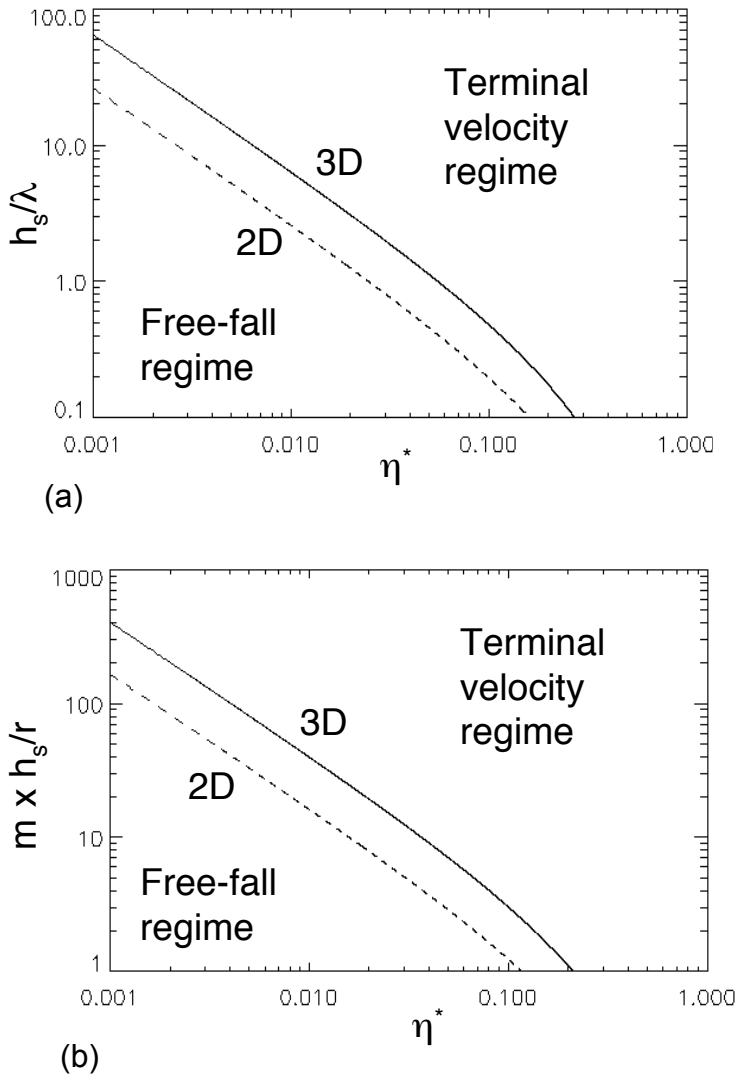

Fig. 9.--Range of validity of the freefall model for spikes at low density ratio: (a) limiting spike amplitude normalized to perturbation wavelength. (b) Limiting mode number for the case of spike amplitude equal to interface radius. At low density ratio, the freefall model remains valid for sufficiently low mode-spikes throughout the fast-growth phase.

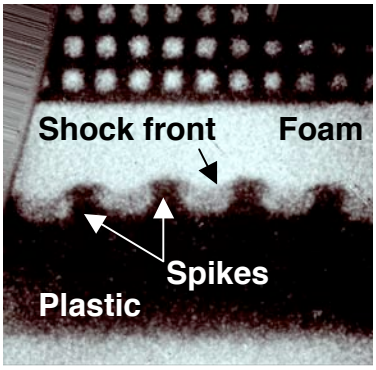

Fig. 10.--X-ray radiograph of a laser-driven planar RM experiment with large initial amplitude ($kh_0 = 0.92$, $\lambda = 150$ μm) [Adapted from Glendinning *et al.* 2003]. A Mach ~ 10 steady shock is incident on a perturbed plastic/foam interface. Due to the large initial amplitude, the RM spike growth speed is higher than the shock recession speed in the interface frame. Consequently, the spikes grow up to and perturb the shock front.

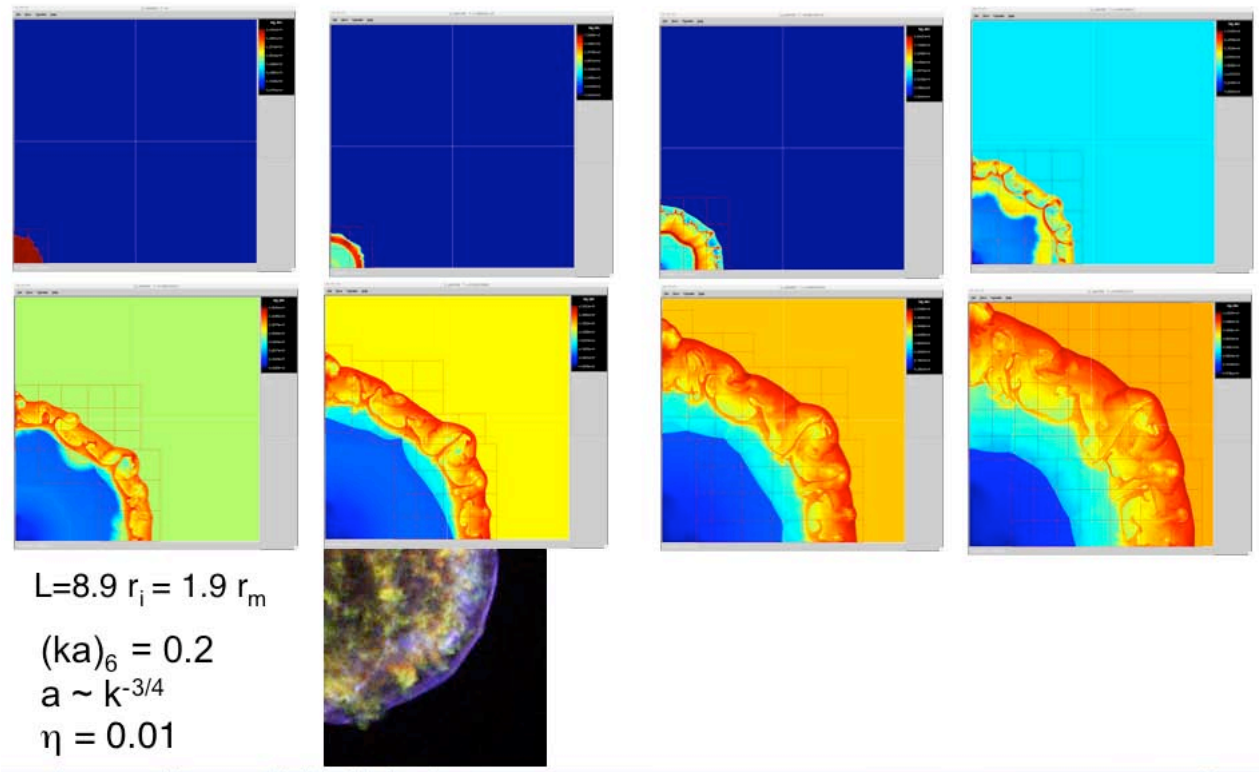

Fig. 11.--Large amplitude low-mode BWI exhibits shock proximity at the scaled Tycho SNR radius [(Forward shock radius)/(Reverse shock radius) ~ 0.7] and shock-interface structure that resembles *Chandra* x-ray data (Warren *et al.* 2005). The initial perturbation spectrum proscribed in the simulation is peaked at mode six with a power law decay to higher mode numbers.

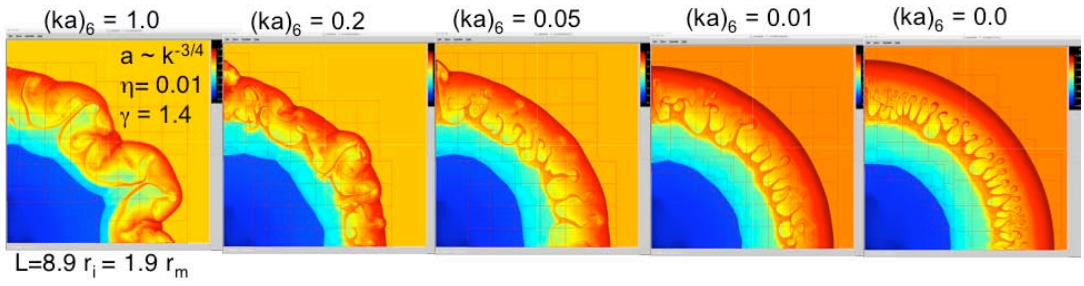

Fig. 12.--Varying the degree of shock proximity by changing the initial amplitude in a series of RAPTOR BWI simulations. At small initial amplitude, the RM contribution to the fast-phase growth is also small and the shock front is smooth. At about the threshold predicted by the planar strong shock relations and impulsive RM model (ka_0 = 0.2 for γ = 1.4), the spikes extend to and perturb the shock front.

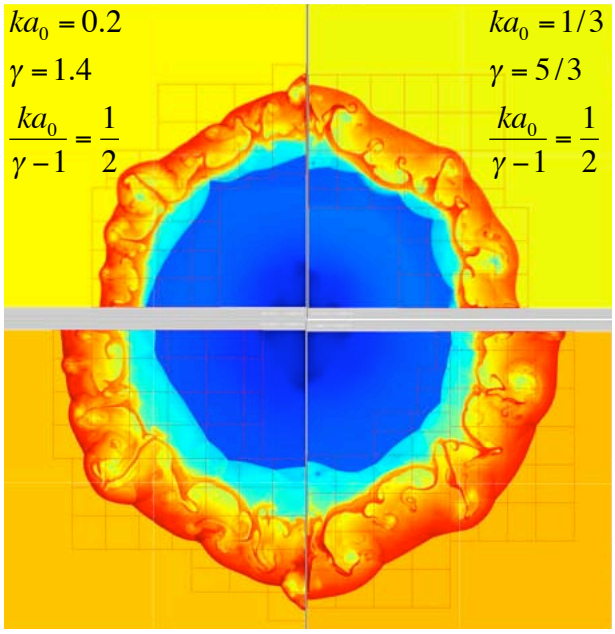

Fig. 13.--Log density plots from a pair of RAPTOR BWI simulations in which the initial amplitude and fluid compressibility are traded off each other while preserving the degree of shock proximity predicted by the planar strong shock relations and impulsive RM model.

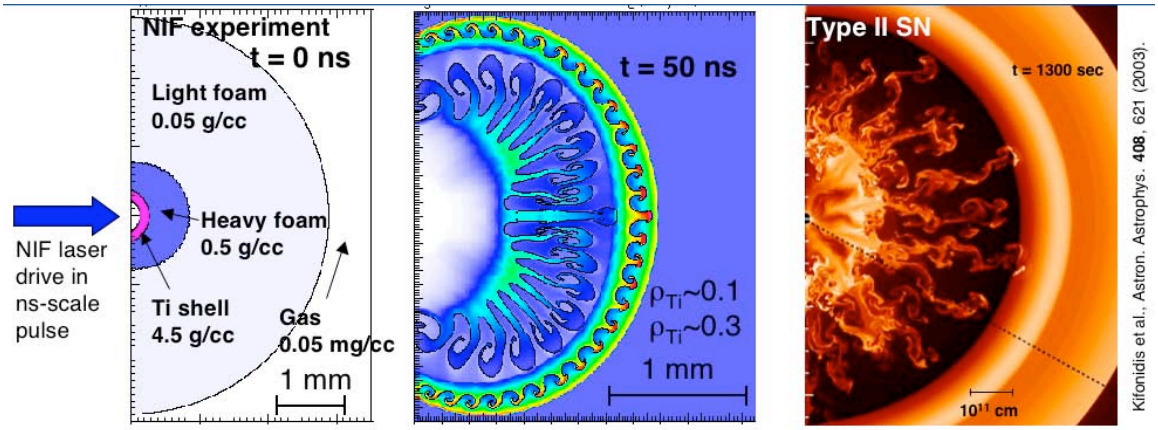

$15M_\odot$ progenitor of		**Fe/Si**	**Si/O**	**(C+O)/He**	**He/H**	**H/ISM**
Kifonidis et al:	**r[km]**	1376	6043	29800	708000	3.5e7
	$M_r/M_\odot$	1.32	1.50	1.68	4.20	15.0
	$M_r/M_{Si/O}$	0.88	**1.00**	1.12	**2.80**	**10.0**
NIF experiment with multiple interfaces at mass-scaled positions			**Ti/(H. foam)**		**(H. foam)/(L. foam)**	**(L. foam)/gas**
	r[μm]		280		855	2883
	$M_r/M_{Ti/CH}$		**1.00**		**2.80**	**10.0**

Fig. 14.--Notional divergent multi-interface Type II SN experiment for the National Ignition Facility laser. Titanium, heavy-foam, and light -oam shells are mass-scaled surrogates for the metal, helium, and hydrogen shells in the progenitor star. Consequently, the evolving structure is comparable to that observed in core-collapse simulations of Kifonidis *et al.* (2003).

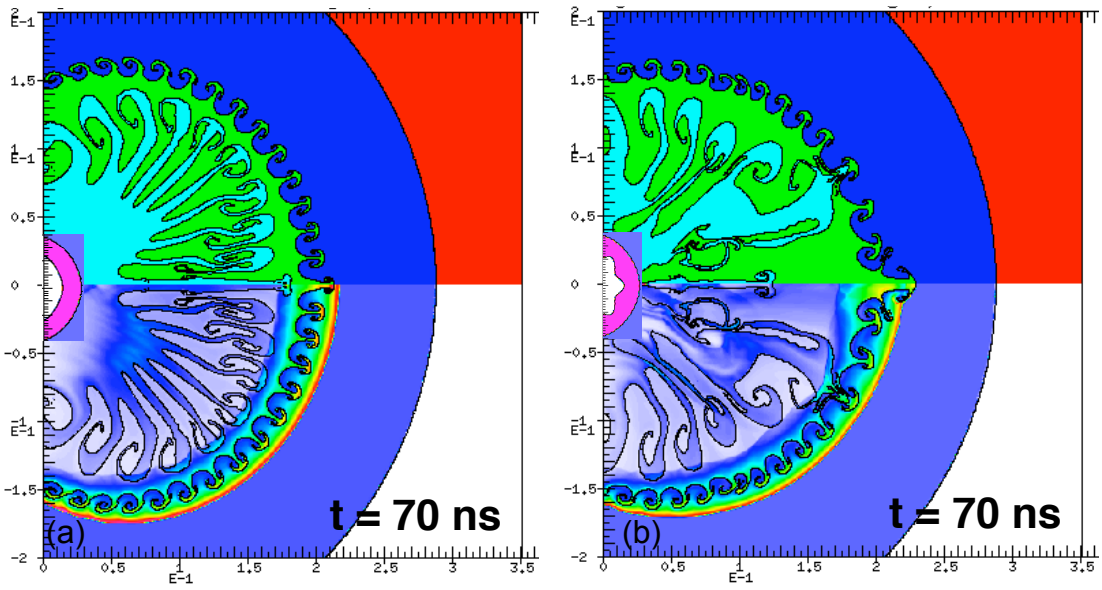

Fig. 15.--Prediction for a pair of laser-drive NIF experiments designed to investigate the effect of having large-amplitude low modes in the initial conditions. In each case, the magenta insert shows the initial Ti inner shell. The lower half of each figure shows density, while the upper half is colored by material: Titanium (core surrogate) is aqua, heavy foam (helium surrogate) is green, and light foam (hydrogen surrogate) is blue. In (b), a large-amplitude mode six pre-imposed on the laser-irradiated surface results in a perturbed shock that transmits that mode to the core/He interface surrogate. This results in enhanced mixing through the surrogate He/H mixing zone.